

The GAPS Programme at TNG

LIX. Characterisation study of the ~300 Myr-old multi-planetary system orbiting the star BD+40 2790 (TOI-2076)[★]

M. Damasso^{1,★★}, D. Locci², S. Benatti², A. Maggio², M. Baratella³, S. Desidera⁴, K. Biazzo⁵, E. Palle^{6,7}, S. Wang⁸, D. Nardiello^{9,4}, L. Borsato⁴, A. S. Bonomo¹, S. Messina¹⁰, G. Nowak^{11,6,7}, A. Goyal⁸, V. J. S. Béjar^{6,7}, A. Bignamini¹², L. Cabona¹³, I. Carleo^{6,7}, R. Claudi⁴, R. Cosentino¹⁴, S. Filomeno^{5,15,16}, C. Knapic¹², N. Lodieu^{6,7}, V. Lorenzi^{14,6}, L. Malavolta^{9,4}, M. Mallorquín^{6,7}, L. Mancini^{15,1,17}, G. Mantovan⁹, G. Micela², F. Murgas^{6,7}, J. Orell-Miquel^{6,7}, M. Pedani¹⁴, M. Pinamonti¹, A. Sozzetti¹, R. Spinelli², M. R. Zapatero Osorio¹⁸, and T. Zingales^{9,4}

(Affiliations can be found after the references)

Received 14 April 2024 / Accepted 8 August 2024

ABSTRACT

Context. The long-term Global Architecture of Planetary Systems (GAPS) programme has been characterising a sample of young systems with transiting planets via spectroscopic and photometric follow-up observations. One of the main goals of GAPS is measuring planets' dynamical masses and bulk densities to help build a picture of how planets evolve in the early stages of their formation via a comparison between the fundamental physical properties of young and mature exoplanets.

Aims. We collected more than 300 high-resolution spectra of the ~300 Myr old star BD+40 2790 (TOI-2076) over about three years. This star hosts three transiting planets discovered by TESS, with orbital periods of ~10, 21, and 35 days. From our determined fundamental planetary physical properties, we investigate the temporal evolution of the planetary atmospheres by calculating the expected mass loss rate due to photo-evaporation up to a system age of 5 Gyr.

Methods. BD+40 2790 shows an activity-induced scatter larger than 30 m s^{-1} in the radial velocities. We employed different methods to measure the stellar radial velocities, along with several models to filter out the dominant stellar activity signal to bring to light the planet-induced signals, which are expected to have semi-amplitudes that are lower by one order of magnitude. We evaluated the mass loss rate of the planetary atmospheres using photo-ionisation hydrodynamic modeling, accounting for the temporal evolution of the stellar high-energy flux through the adoption of different models for X-rays and EUV irradiation.

Results. The dynamical analysis confirms that the three sub-Neptune-sized companions (with our radius measurements of $R_b = 2.54 \pm 0.04$, $R_c = 3.35 \pm 0.05$, and $R_d = 3.29 \pm 0.06 R_{\oplus}$) have masses that situate them in the planetary regime. We derived 3σ upper limits below or close to the mass of Neptune for all the planets in our sample: 11–12, 12–13.5, and 14–19 M_{\oplus} for planets *b*, *c*, and *d*, respectively. In the case of planet *d*, we found promising clues that the mass could be between ~7 and 8 M_{\oplus} , with a significance level between 2.3–2.5 σ (at best). This result must be further investigated using other analysis methods and techniques or using high-precision near-infrared (nIR) spectrographs to collect new radial velocities, which could be less affected by stellar activity. Atmospheric photo-evaporation simulations predict that BD+40 2790 b is currently losing its H-He gaseous envelope and that it will be completely lost at an age within 0.5–3 Gyr if its current mass is lower than 12 M_{\oplus} . Furthermore, BD+40 2790 c could have a lower bulk density than *b* and might be able to retain its atmosphere up to an age of 5 Gyr. For the outermost object, planet *d*, we predicted an almost negligible evolution of its mass and radius, induced by photo-evaporation.

Key words. techniques: photometric – techniques: radial velocities – planets and satellites: general – stars: individual: BD+40 2790

1. Introduction

For more than five years, the Global Architecture of Planetary Systems (GAPS) collaboration (Covino et al. 2013) has carried out a radial velocity (RV) survey to search for and characterise planets around young stars (i.e. with an age less than

~800 Myr) within the Young Objects (YO) sub-programme (e.g. Carleo et al. 2020; Benatti et al. 2023b). The main goal of the survey is measuring the fundamental orbital and physical properties of planetary systems during their early life stages, when most of the processes that shape their final architectures occur. The typical mechanisms that leave some imprints on the system properties include planetary migration (e.g. Ford & Rasio 2008; Cossou et al. 2014; Baruteau et al. 2014), tidal circularisation (e.g. Jackson et al. 2008; Chatterjee et al. 2008), and photo-evaporation (e.g. Owen & Wu 2013). Along with GAPS, other RV surveys like ZEIT (Mann et al. 2016a), THYME (Newton et al. 2019), and RVSPY (Zakhochay et al. 2022), or observational campaigns focused on specific targets (e.g. Lillo-Box et al. 2020; Cale et al. 2021; Barragán et al. 2022b;

[★] Based on observations made with i) the Italian Telescopio Nazionale Galileo (TNG) operated by the Fundación Galileo Galilei (FGG) of the Istituto Nazionale di Astrofisica (INAF) at (i) the Observatorio del Roque de los Muchachos (La Palma, Canary Islands, Spain); (ii) the Spanish 3.5 m telescope at Calar Alto Observatory (Almería, Spain); (iii) the US WIYN 3.5 m telescope at Kitt Peak National Observatory (Tucson, Arizona).

^{★★} Corresponding author; mario.damasso@inaf.it

Mallorquín et al. 2023) pursued a similar goal. The current observational scenario indicates that small planets with a gaseous envelope on close-in orbits around stars younger than ~ 150 Myr show inflated radii, as previously suggested by Kraus et al. (2015) and Mann et al. (2016b). At this stage, they are subject to the Kelvin-Helmholtz contraction and possibly to the photo-evaporation of their atmosphere, as shown in the simulations discussed, for instance, by Maggio et al. (2022). This condition leads to a decrease in the radii and, as a consequence, we can expect an evolution of the location on a mass-radius with the age of the systems. This hypothesis requires the follow-up of a larger sample of young planets to be effectively tested (see e.g. Benatti et al. 2023a). The main reason to explain the current relative scarcity of young exoplanets followed-up with the RV method is the intrinsic difficulty in obtaining robust mass measurements due to the effects of the stellar activity that can impact the modelling of RV data in a severe way.

The experience gleaned within the GAPS-YO survey suggests that aiming for accurate measurements of planetary masses requires the collection of a considerable number of observations per target, possibly spanning several seasons and with a cadence dense enough to guarantee a good data sampling over the stellar rotational cycles. In fact, this can be a preferred way to obtain a proper treatment and mitigation of the stellar activity with state-of-the-art data modelling tools. This is particularly true in the cases of small-size planets or multi-planet systems. Despite the greater challenges in measuring the planetary masses due to the multiplicity of Doppler signals present in the RV time series, multi-planet systems represent a valuable resource for comparative planetology; for example, by investigating the effects of the photo-evaporation as a function of the distance from the host stars (e.g. Carleo et al. 2021; Damasso et al. 2023) and those induced on the planetary formation and migration mechanisms by the presence of multiple bodies in a system (e.g. Turrini et al. 2023; Mantovan et al. 2024).

In this paper, we present a characterisation study of the ~ 300 Myr old multi-planetary system orbiting the K-type star BD+40 2790, also known as TOI-2076, based on photometric and high-resolution spectroscopic observations. The discovery and validation of three transiting sub-Neptune-sized planets (with orbital periods ~ 10 , 21, and 35 days) by using photometric data collected by the Transiting Exoplanet Survey Satellite (TESS; Ricker et al. 2015) was presented by Hedges et al. (2021). As only two non-consecutive transits were observed for the two outer planets *c* and *d*, the TESS data were not sufficient to calculate their orbital periods and constrain their orbits. Thanks to observations with the CHAracterising ExOPlanets Satellite (CHEOPS) space telescope and a ground-based follow-up, Osborn et al. (2022) were able to pin down the orbital periods of BD+402790 *c* and *d*. They found a period ratio close to 5:3 for BD+402790 *c* and *d*, and an anti-correlated transit timing variation (TTV) signal between planets *b* and *c*, likely linked to the 2:1 ratio of their orbital periods. Osborn et al. (2022) revised the radius measurements of the planets, revealing that all of them fall in the sub-Neptune size range. By modeling the Rossiter–McLaughlin effect of TOI-2076 *b*, Frazier et al. (2023) found that the planet has a low sky-projected obliquity, concluding that a well-aligned orbit, together with the presence of TTVs, suggests that the compact multi-planet system likely evolved through disk migration in an initially well-aligned disk. In the attempt to search for atmospheric escape from young sub-Neptunes with Keck/NIRSPEC, Zhang et al. (2023) reported the detection of helium absorption in the atmosphere of TOI-2076 *b*, whose observed properties appear consistent with the

expectations from photo-evaporation. However, Gaidos et al. (2023) observed helium excess absorption during the same transit as in Zhang et al. (2023) and argued that this is stellar in origin.

In this study, we employ an RV sample composed by more than 300 data points, which have been collected using three high-resolution spectrographs, with the main goal of measuring dynamical masses and bulk densities of the three planets. In Section 2, we describe the photometric and spectroscopic dataset, which we also used to revise the fundamental stellar parameters, as discussed in Section 3. In Section 4, we investigate which are the significant periodic signals in our spectroscopic and photometric dataset. We made use of the results to set up a thorough modelling of the data described in Section 5. We investigate in Sect. 6 the planetary atmospheric evolution through models based on photo-evaporation and we summarise our results in Sect. 7.

2. Description of the dataset

2.1. TESS photometric observations

TESS observed TOI-2076 during Cycle 2 (in Sectors 16, from 11 September to 6 October 2019, and Sector 23, from 19 March to 15 April 2020) and during Cycle 4 (in Sector 50, from 26 March to 22 April 2022). This star belongs to the list of targets of the Guest Investigator programs GO-4195 (PI: Villanueva), GO-4231 (PI: Dragomir), GO-4023 (PI: Kipping), GO-4191 (PI: Burt), GO-4242 (PI: Mayo), and GO-4039 (PI: Davenport). An analysis of the complete TESS dataset is presented in Zhang et al. (2023).

In our work, we used the short-cadence light curve (two-minute sampling). As already done in previous works of the GAPS series, we did not adopt the pre-search data conditioning simple aperture photometry (PDCSAP, Smith et al. 2012; Stumpe et al. 2012, 2014) light curves, because they could be affected by systematics due to over-corrections and/or injection of spurious signals. Instead, by using the cotrending basis vectors extracted as in Nardiello et al. (2021, 2022), we corrected the simple aperture photometry (SAP) light curve. The resulting light curve, with the transits removed, is shown in Fig. 1.

The measurement of the planetary radii from light curves of young and active stars can be influenced by the choice of the algorithm used to model and remove the variability due to the stellar activity (e.g. see Canocchi, G. et al. 2023). To this purpose, we used the publicly available Python package `wotan`¹ (Hippke et al. 2019) to detrend (or flatten) the TESS light curve. From `wotan`, we selected the `cosine` (a sum of sines and cosines, with an iterative clipping of 2σ outliers until convergence) and `hspline` (spline with a robust Huber estimator) from the available algorithms. The transits of the three planets were masked before detrending the light curve using the ephemeris reported by Osborn et al. (2022), then the derived model of stellar activity was interpolated to the in-transit data points, and the original light curve flattened. In Sect. 5.1, we compare the radius measurements obtained from the analysis of these two versions of the light curve, to inspect whether there are significant differences due to the choice of a specific detrending algorithm over the other.

2.2. Analysis of additional archival photometry

For the measurement of the stellar rotation period, $P_{\text{rot}, \star}$, for which Nardiello et al. (2022) provided a measurement based on

¹ <https://github.com/hippke/wotan>

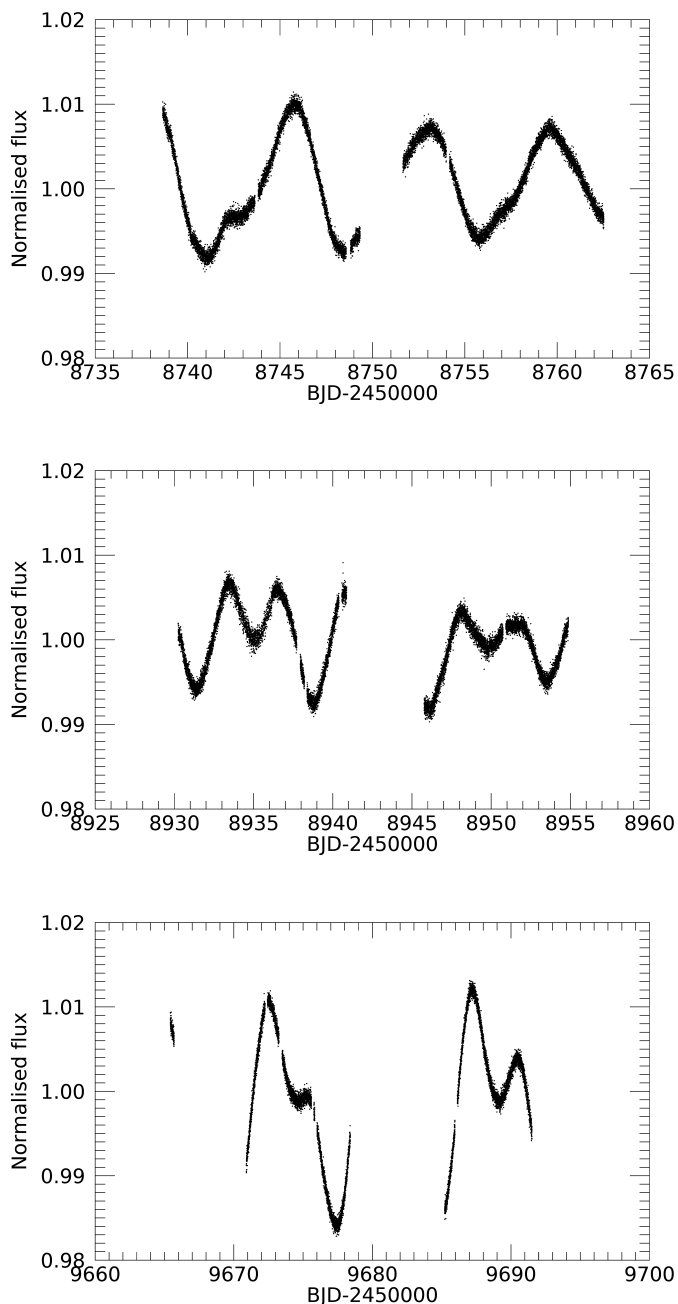


Fig. 1. TESS light curves of Sectors 16, 23, and 50, which were extracted as described in Sect. 2.1, shown from top to bottom. The transits of the three planets were masked and bad-quality points were removed.

TESS data ($P_{\text{rot}, \star} = 7.29 \pm 0.12$ d), we made use of additional archive datasets of adequate photometric precision and a longer baseline with respect to the TESS observations. We made use of the All-Sky Automated Survey for SuperNovae (ASAS-SN; Shappee et al. 2014; Kochanek et al. 2017) V-band observations. We downloaded the light curve from the public archive² and we removed low-quality data and all the points associated with a seeing larger than 3σ the mean seeing of each photometric series. The photometric series of TOI-2076 spans from March 2013 to August 2018 (765 points).

² <https://asas-sn.osu.edu/>

We also analysed the publicly available light curves obtained by the SuperWASP survey (Pollacco et al. 2006; Butters et al. 2010), after removing from the time series the data with the quality flag FLAG=0 (not-corrected photometric points) and outliers.

2.3. HARPS-N spectroscopic observations

TOI-2076 was observed with the HARPS-N spectrograph (Cosentino et al. 2012), mounted at the Telescopio Nazionale Galileo (TNG) on the island of La Palma (Canary Islands, Spain), from 6 August 2020 to 14 September 2022, with exposure times of 900s or 1200s. The spectra have a median S/N of 93 measured at a wavelength of ~ 550 nm. Nearly 96% of the total amount of spectra have been collected within the GAPS programme, but TOI-2076 was also followed-up during Spanish CAT time allocations (CAT19A_162, PI: Nowak; ITP19_1 PI Pallé). The merged sample consists of 294 spectra. We excluded from the dataset the spectrum taken at epoch BJD 2459286.697138 with low S/N (< 25).

We adopted three different algorithms to extract the RVs from the HARPS-N spectra, with the purpose of testing their relative sensitivity to stellar activity contamination. In our study, we analyse all these alternative HARPS-N RV datasets with the same set of test models. We used the standard Data Reduction Software (DRS) pipeline (version 3.7.0) through the YABI workflow interface (Hunter et al. 2012), which is maintained by the Italian center for Astronomical Archive (IA2)³. The RVs and activity diagnostics full width at half maximum (FWHM) and bisector inverse slope (BIS) were derived from the DRS cross-correlation function (CCF), which was calculated by adopting a reference mask for a star with spectral type K5 and a half-window width of 30 km s^{-1} .

We extracted a second version of the RV dataset using the code SERVAL (spectrum radial velocity analyser, version dated 26 January 2022; Zechmeister et al. 2018), which adopts a procedure based on template-matching to derive relative RVs⁴. Using SERVAL, we calculated the RVs using both all the echelle orders, but also selecting specific echelle orders (wavelength ranges) for the computation of a ‘chromatic’ RV dataset, as detailed in Table 1. Our goal is to test whether we can reduce the RV scatter due to stellar activity by excluding ‘bluer’ orders of the full wavelength range covered by HARPS-N ($\sim 3800 \text{ \AA}$ to 6900 \AA) and, ultimately, to verify if a reduced activity contamination can help to retrieving the planetary-induced Doppler signals. A wavelength dependence in the activity-induced RV scatter could be expected for young and active stars whose photosphere is spot-dominated, with the amplitude decreasing in the redder parts of the spectrum (e.g. Prato et al. 2008; Mahmud et al. 2011; Carleo et al. 2020). For our empirical test, we selected four different subsets of echelle orders and we focused on the dataset corresponding to the wavelength range from $\sim 5393 \text{ \AA}$ to $\sim 6916 \text{ \AA}$ to perform an analysis with all the test models adopted in this study (Sect. 5.2 and Appendix B). The other ‘chromatic’ datasets have been analysed only with a subset of the test models to compare the results obtained especially for planet TOI-2076 d. From Table 1, we note that the RV root mean square (rms) decreases when ‘bluer’ orders are progressively

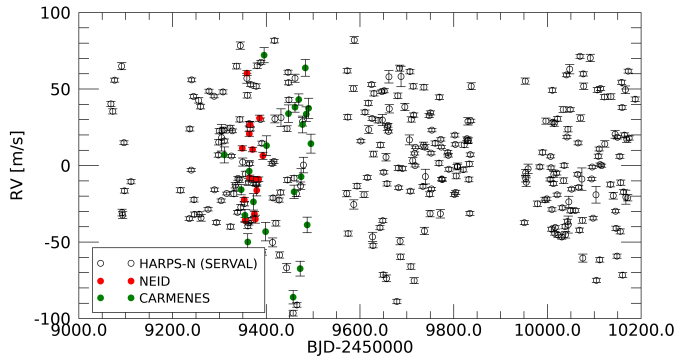
³ <https://www.ia2.inaf.it/>

⁴ The code is publicly available at <https://github.com/mzechmeister/serval>. We used `-snmin 10.0 -niter 2 -safemode` as keywords in calling the software procedure, and the keyword `-oset` to select a specific subset of echelle spectral orders for the RV computation.

Table 1. Summary of the different RV datasets analysed in this work.

Instrument	Nr. of data	Time span (BJD-2450000)	RV rms (m s ⁻¹)	median σ_{RV} (m s ⁻¹)
HARPS-N, all orders (SERVAL)	293	9068.41–10187.36 [1119 d]	36.0	1.5
HARPS-N, wavelength range nr. 1 (SERVAL; from $\sim 4014 \text{ \AA}$ to $\sim 5393 \text{ \AA}$) ^(a)	293	9068.41–10187.36 [1119 d]	37.4	1.8
HARPS-N, wavelength range nr. 2 (SERVAL; from $\sim 4800 \text{ \AA}$ to $\sim 6916 \text{ \AA}$) ^(b)	293	9068.41–10187.36 [1119 d]	34.6	1.9
HARPS-N, wavelength range nr. 3 (SERVAL; from $\sim 5393 \text{ \AA}$ to $\sim 6916 \text{ \AA}$) ^(c)	293	9068.41–10187.36 [1119 d]	32.9	2.8
HARPS-N, wavelength range nr. 4 (SERVAL; from $\sim 5695 \text{ \AA}$ to $\sim 6916 \text{ \AA}$) ^(d)	293	9068.41–10187.36 [1119 d]	32.5	3.7
HARPS-N, all orders (DRS)	293	9068.41–10187.36 [1119 d]	34.7	1.6
HARPS-N, all orders (LBL)	293	9068.41–10187.36 [1119 d]	36.6	1.5
NEID	15	9348.80–9392.83 [44 d]	27.4	1.7
CARMENES-VIS	22	9310.63–9495.29 [185 d]	42.2	5.3

Notes. ^(a)This wavelength range corresponds to pipeline-wise echelle orders from 6 to 43. ^(b)This wavelength range corresponds to pipeline-wise echelle orders from 30 to 69. ^(c)This wavelength range corresponds to pipeline-wise echelle orders from 44 to 69. ^(d)This wavelength range corresponds to pipeline-wise echelle orders from 50 to 69.


Fig. 2. RV time series analysed in this work. For HARPS-N, data extracted with SERVAL (all echelle orders) are shown.

excluded from the RV computation, at the cost of increasing the RV uncertainties, σ_{RV} .

Recently, Artigau et al. (2022) proposed a line-by-line (LBL) algorithm for high-precision RV measurements. We applied the algorithm LBL⁵ to our HARPS-N spectra as a further test to evaluate the performances of a different RV extraction method for a star with a high level of activity-induced RV scatter.

HARPS-N data represents the bulk of the spectroscopic dataset analysed in this work. We also used data collected by CARMENES and NEID spectrographs, described in Appendix A. In Fig. 2, we show the time series of the combined RV datasets and their properties are summarised in Table 1. The RV datasets are available online at CDS.

3. Stellar fundamental parameters

3.1. Photometric T_{eff} and reddening

From the colte package (Casagrande et al. 2021) and considering the *Gaia* DR3 and 2MASS photometry, we estimated a

⁵ We used version 0.63 of the publicly available Python code (<https://github.com/njcuk9999/lbl>), following a standard recipe to run the algorithm, as described in the online repository, using all the echelle spectral orders.

weighted mean temperature of $5180 \pm 45 \text{ K}$ from the calibration relations based on different colour indices, with T_{eff} ranging from $5122 \pm 56 \text{ K}$ in the $G - B_p$ colour index up to $5227 \pm 60 \text{ K}$ for $G - R_p$. We used this value as an initial guess for the spectroscopic determination of T_{eff} , as described in Sect. 3.2. Reddening toward TOI-2076 is negligible, which can be seen in the maps from Montalto et al. (2021) and the expectation given the short distance from the Sun (42.0 pc). From the spectral energy distribution, there are no indications of the presence of significant infrared (IR) excess.

3.2. Spectroscopic analysis

TOI-2076 is a young ($\sim 300 \text{ Myr}$ old) star (see Sect. 3.7), for which the intense magnetic activity can modify the structure of the stellar photosphere, thus altering the shape of the spectral lines formed in the upper layers. This effect could be particularly evident for iron (Fe) lines, which are typically used to derive the stellar parameters with the standard method based on line equivalent widths (EWs; see, e.g. Yana Galarza et al. 2019; Spina et al. 2020). As a consequence, when micro-turbulence velocity ξ is derived by imposing the same iron abundance for weak and strong Fe lines, this could lead to an overestimation of ξ and, therefore, to an underestimation of the iron abundances [Fe/H]. To avoid these issues, we considered the procedure developed by Baratella et al. (2020b) and based on the use of titanium (Ti) lines to derive the surface gravity ($\log g$) and ξ . Titanium lines typically form deeper in the photosphere compared to Fe lines and are less influenced by the effects of the magnetic fields, as seen on Fe transitions which show EWs that are 5–10 mÅ larger in young, active solar analogue stars (see Fig. 9 in Baratella et al. 2020b), allowing for a measurement of ξ not correlated with stellar activity. We used a combination of Fe and Ti lines to derive the effective temperature (T_{eff}), adopting the Ti and Fe line list published by Baratella et al. (2020a) and measuring the line EWs through the software ARESv2 (Sousa et al. 2015), discarding those lines with errors larger than 10% and with $\text{EW} > 120 \text{ mÅ}$.

As our initial guess for the spectroscopic analysis, we took the photometric $T_{\text{eff,phot}}$ derived above (i.e. $5180 \pm 45 \text{ K}$), $\log g$ from *Gaia* parallax ($4.59 \pm 0.08 \text{ dex}$), and microturbulence

velocity $\xi = 0.80 \pm 0.04 \text{ km s}^{-1}$ from the calibration of Dutra-Ferreira et al. (2016).

We thus created the 1D LTE model atmosphere linearly interpolated from the ATLAS9 grid of Castelli & Kurucz (2003) with new opacities (ODFNEW) and used the driver *abfind* of MOOG Sneden (1973) for deriving the following final spectroscopic parameters: $T_{\text{eff,spec}} = 5200 \pm 100 \text{ K}$, $\log g_{\text{spec}} = 4.52 \pm 0.05 \text{ dex}$, $\xi_{\text{spec}} = 0.90 \pm 0.10 \text{ km s}^{-1}$, and $[\text{Fe}/\text{H}] = -0.03 \pm 0.06$ (see Table 2). Our spectroscopic parameters agree well with the input estimates and with those published by Osborn et al. (2022). $T_{\text{eff,spec}}$ is in agreement with $T_{\text{eff,photo}}$, although less precise. Nonetheless, we prefer to adopt the more conservative $T_{\text{eff,spec}}$ as our reference value, in that it is derived, together with the other atmospheric parameters, using a method optimised for young and active stars, that robustly account for systematics. Overall, the star has solar elemental abundances (see Filomeno et al. 2024).

3.3. Lithium

We measured the equivalent width of the Li line at 6707.8 \AA , using the IRAF task *splot*. Its value resulted to be $89.8 \pm 1.0 \text{ m\AA}$, where the error was estimated from the standard deviation of three EW measurements. Then, we also derived the NLTE Li abundance through the prescriptions by Lind et al. (2009) and by adopting the spectroscopic parameters from Sect. 3.2. Final lithium abundance $\log A(\text{Li})^{\text{NLTE}}$ is $2.11 \pm 0.10 \text{ dex}$, where uncertainty was estimated considering both the errors on EW and on spectroscopic parameters (see Table 2). We find very similar values also applying the spectral synthesis method (see Biazzo et al. 2022). Our Li abundance is intermediate between the Pleiades open cluster and the Ursa Major association, fully compatible with the group membership and age derived by Nardiello et al. (2022) (see also Sect. 3.7).

3.4. Projected rotational velocity

Using the spectroscopic stellar parameters derived above, the driver *synth* of MOOG (Sneden 1973) and the Castelli & Kurucz (2003) grid of model atmospheres, we also measured the projected rotational velocity ($v \sin i$) through the synthesis of three spectral regions around 5400 , 6200 , and 6700 \AA . Assuming a macroturbulence velocity $v_{\text{macro}} = 2.05 \text{ km s}^{-1}$ from the relations by Brewer et al. (2016), we found a final value of $v \sin i_{\star} = 5.2 \pm 0.4 \text{ km s}^{-1}$ (see Table 2).

Rainer et al. (2023) determined a linear relation to derive the projected rotational velocity of a star from the FWHM of the CCF (see Eq. (7) therein calculated for a K5 mask). Using this calibration, we obtain $v \sin i_{\star} = 5.2 \pm 2.4 \text{ km s}^{-1}$, assuming the weighted mean of all the FWHM measurements and the median of the associated errors as a reference value (FWHM = $8.8412 \pm 0.0032 \text{ km s}^{-1}$) and taking into account the errors of the coefficients in the calibration formula. This value is in agreement with the measurement from the spectral synthesis, although less precise.

3.5. Stellar rotation period

Hedges et al. (2021) derived a stellar rotation period $P_{\text{rot},\star} = 7.27 \pm 0.23$ days from the analysis of TESS (Sectors 16 and 23) and KELT light curves. We use our extracted TESS light curve, including Sector 50, to redetermine $P_{\text{rot},\star}$. The light curve was analysed with the CLEAN algorithm (Roberts et al. 1987)

Table 2. Stellar parameters of BD+40 2790 (TOI-2076).

Parameter	Value	Ref
α (J2000)	14:29:34.24	(Gaia Collaboration 2016, 2021)
δ (J2000)	+39:47:25.54	(Gaia Collaboration 2016, 2021)
μ_{α} (mas/yr)	-118.071±0.010	(Gaia Collaboration 2016, 2021)
μ_{δ} (mas/yr)	-6.860±0.013	(Gaia Collaboration 2016, 2021)
π (mas)	23.8052 ± 0.0125	(Gaia Collaboration 2016, 2021, 2023)
B_T (mag)	10.258 ± 0.025	(Høg et al. 2000)
V_T (mag)	9.238 ± 0.015	(Høg et al. 2000)
G (mag)	8.918 ± 0.003	(Gaia Collaboration 2016, 2021, 2023)
Gaia BP	9.349±0.003	(Gaia Collaboration 2016, 2021, 2023)
Gaia RP	8.319±0.004	(Gaia Collaboration 2016, 2021, 2023)
$J_{2\text{MASS}}$ (mag)	7.613 ± 0.019	(Cutri et al. 2003)
$H_{2\text{MASS}}$ (mag)	7.188 ± 0.027	(Cutri et al. 2003)
$K_{2\text{MASS}}$ (mag)	7.115 ± 0.017	(Cutri et al. 2003)
WISE1 (mag)	7.011 ± 0.050	(Cutri et al. 2021)
WISE2 (mag)	7.126 ± 0.019	(Cutri et al. 2021)
WISE3 (mag)	7.092 ± 0.016	(Cutri et al. 2021)
WISE4 (mag)	7.003 ± 0.089	(Cutri et al. 2021)
T_{eff} (K)	5200±100	This paper (spectroscopic; adopted)
T_{eff} (K)	5180±45	This paper (photometric)
$\log g$	4.52±0.05	This paper
[Fe/H] (dex)	-0.03±0.06	This paper
E(B-V)	0.003±0.015	PIC (Montalto et al. 2021)
S_{MW}	0.548 ± 0.027	This paper (HARPS-N spectra)
$\log R'_{\text{HK}}$	-4.354 ± 0.025	This paper (HARPS-N spectra)
$v \sin i_{\star}$ (km/s)	5.2±0.4	This paper
L_{bol} (L_{\odot})	0.383 ± 0.013	This paper
$P_{\text{rot},\star}$ (d)	7.31±0.03	This paper
L_X (erg/cm ²)	$5.6^{+2.5}_{-1.0} \times 10^{28}$	This paper
$\log L_X/L_{\text{bol}}$	$-4.42^{+0.16}_{-0.09}$	This paper
A(Li)	2.11±0.10	This paper
Mass (M_{\odot})	$0.849^{+0.027}_{-0.026}$	This paper
Radius (R_{\odot})	0.758 ± 0.014	This paper
Density (g cm ⁻³)	$2.74^{+0.15}_{-0.14}$	This paper
Age (Myr)	300 ± 80	Nardiello et al. (2022)

and we derived $P_{\text{rot},\star} = 7.3 \pm 1.1 \text{ d}$ with a very high confidence level in all the individual sectors. An improved period determination comes from the analysis of the combined sectors, that is, $P_{\text{rot},\star} = 7.31 \pm 0.03 \text{ d}$, and we assume this as our reference value. In Fig. C.1 we show the CLEAN periodograms for each sector and for their combination. We note a significant power peak, although smaller than the primary, at about half the rotation period, which arises from the presence of a secondary minimum in the light curve, whose amplitude evolves with time, reaching the maximum depth in Sector 23.

We also analysed archival light curves from ASAS-SN and SuperWASP as a cross-check. The analysis of the periodogram of the ASAS-SN light curve resulted in a peak at $P = 7.53 \text{ d}$, with low power ($Pw \sim 0.04$). From the analysis of the periodogram of the SuperWASP light curve, we measured a single significant peak at a period, $P = 7.33 \text{ d}$ ($Pw \sim 0.15$).

3.6. Coronal and chromospheric activity

The HARPS-N data allowed us to determine a mean value of the chromospheric index $\log R'_{\text{HK}} = -4.354 \pm 0.025$ (Sect. 4). We

employed this value and its uncertainty to estimate the X-ray luminosity of TOI-2076, with the scaling law by Mamajek & Hillenbrand (2008), obtaining $\log L_x = 28.86^{+0.09}_{-0.08} \text{ erg s}^{-1}$. Using the calibration with the stellar age by the same authors, we found that the predicted $\log R'_{\text{HK}}$ is in the range $-4.38^{+0.04}_{-0.03}$ for an age of $300 \pm 80 \text{ Myr}$. This is in good agreement with the measurements.

The only direct measurement of the X-ray luminosity of TOI-2076 currently available is based on a faint detection of this source in the ROSAT All-Sky Survey, leading to $\log L_x = 28.67 \pm 0.16 \text{ erg s}^{-1}$ (Hedges et al. 2021). This value is lower but in agreement within the error bars than that derived from the measured chromospheric Ca II H&K index.

We obtained an alternative estimate of the X-ray luminosity starting from the mean rotation period of $P = 7.31 \pm 0.03 \text{ d}$ (Table 2) and adopting the activity–rotation relationships by Pizzolato et al. (2003), yielding $\log L_x = 28.75 \pm 0.01 \text{ erg s}^{-1}$; this is just $\sim 20\%$ lower and within 2σ with respect to the value derived from the chromospheric index and the stellar age. We adopted this as the reference value for investigating the photo-evaporation histories of the planets in this system (Sect. 6).

However, we also verified that this X-ray luminosity corresponds to the 2% percentile of the distribution expected for stars with the same mass and age of TOI-2076, while the rotation period corresponds to the 45% percentile of the related distribution (Johnstone et al. 2021). In conclusion, the coronal emission level appears to be in the low-end tail of the expected distribution for stars similar to TOI-2076.

3.7. Membership to group and stellar age

TOI-2076 has very similar kinematic parameters and age to the young star TOI-1807 (Hedges et al. 2021). Their membership to the same comoving group was confirmed by Nardiello et al. (2022), who found that TOI-2076 has a rotation period matching well the rotational sequence of the group (Fig. 7 in Nardiello et al. 2022). In this study we adopt for TOI-2076 the robust age that Nardiello et al. (2022) determined for the comoving group, namely $300 \pm 80 \text{ Myr}$.

3.8. Binarity

Beside the co-moving objects discussed in Nardiello et al. (2022), which are at physical separations too wide for being gravitationally bound to TOI-2076, there are no indications of close massive companions from *Gaia* astrometry (Gaia Collaboration 2016) using data from DR3 (RUWE = 0.98; Gaia Collaboration 2021, 2023), direct imaging (Gaia and AO observations by Hedges et al. 2021), our own four-yr RV time series, and long-term proper motion differences (less than two σ for Tycho2 and *Gaia* DR3).

3.9. Mass, radius, and luminosity from SED analysis

We determined the stellar radius and mass with the EXOFASTv2 tool (Eastman et al. 2019), by fitting the stellar spectral energy distribution (SED). The stellar luminosity calculated from the SED has been provided as input to the MIST stellar evolutionary tracks (Dotter 2016). For the SED fitting, we considered the Tycho *B* and *V* magnitudes (Høg et al. 2000), the 2MASS near-IR *J*, *H*, and *K* magnitudes (Cutri et al. 2003), and the WISE mid-IR *W1*, *W2*, *W3*, and *W4* magnitudes (Cutri et al. 2021). We imposed Gaussian priors on (i) the stellar effective temperature, T_{eff} , and metallicity, $[\text{Fe}/\text{H}]$, from our analysis of the HARPS-N spectra, (ii) the parallax $23.8052 \pm 0.0125 \text{ mas}$ from the *Gaia*

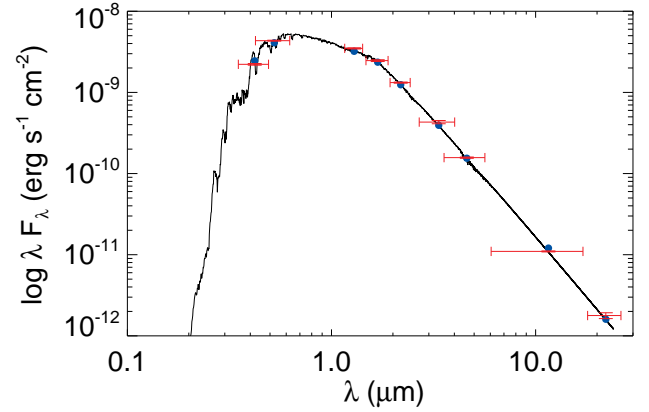


Fig. 3. Spectral energy distribution of BD+40 2790 (TOI-2076) with the best-fit model overplotted (solid line). Red and blue points correspond to the observed and predicted values, respectively.

DR3, and (iii) the stellar age $300 \pm 80 \text{ Myr}$ from Nardiello et al. (2022). We used uninformative priors for all the other parameters. The best fit of the SED is shown in Fig. 3. We found $M_\star = 0.849^{+0.027}_{-0.026} M_\odot$ and $R_\star = 0.758 \pm 0.014 R_\odot$. The derived mass is in agreement with the prediction of the PAdova TRIeste Stellar Evolutionary Code (PARSEC) models (Bressan et al. 2012).

Coupling the measured stellar radius and rotation period yields an equatorial velocity of 5.24 km s^{-1} . This is very close to the observed $v \sin i_\star$, further supporting the edge-on inclination of the star obtained through the Rossiter-McLaughlin effect by Frazier et al. (2023).

4. Frequency content analysis of RVs and activity diagnostics

In our study, we analysed the time series of three activity diagnostics calculated from HARPS-N spectra, namely BIS, FWHM, and $\log R'_{\text{HK}}$. The FWHM and $\log R'_{\text{HK}}$ time series show by eye a possible long-term modulation per cycle, which is confirmed by calculating the generalised Lomb-Scargle (GLS; Zechmeister & Kürster 2009) periodograms shown in Fig. 4. Both show significant peaks, with a false alarm probability (FAP) lower than 0.1%, with the highest power around 1000 days. The statistical FAP has been evaluated through 10 000 bootstrap (with replacement) simulations. The periodograms of the pre-whitened time series show peaks at the stellar rotation period and its first and second harmonic (for the FWHM) and at the rotation period (for the $\log R'_{\text{HK}}$). The periodogram of the BIS index does not show peaks at low frequencies and it is dominated by the first harmonic of the stellar rotation period.

The upper panel of Fig. 4, and plots of Fig. C.2, show the GLS periodograms of HARPS-N RVs extracted with different algorithms (Table 1). In all the cases, dominant and statistically significant peaks are found at $P_{\text{rot}, \star}$ and its first harmonic, clearly denoting that the observed RV scatter $> 30 \text{ m s}^{-1}$ is mostly due to stellar activity, which must be filtered out in the attempt to detect the Doppler signals related to the planets in the system. In Fig. 5, we show the RVs phase folded to $P_{\text{rot}, \star}$ for three sub-samples to highlight how the variability induced by the stellar activity changes on a seasonal basis. There are no significant peaks at low frequencies, contrary to what is observed for the FWHM and $\log R'_{\text{HK}}$.

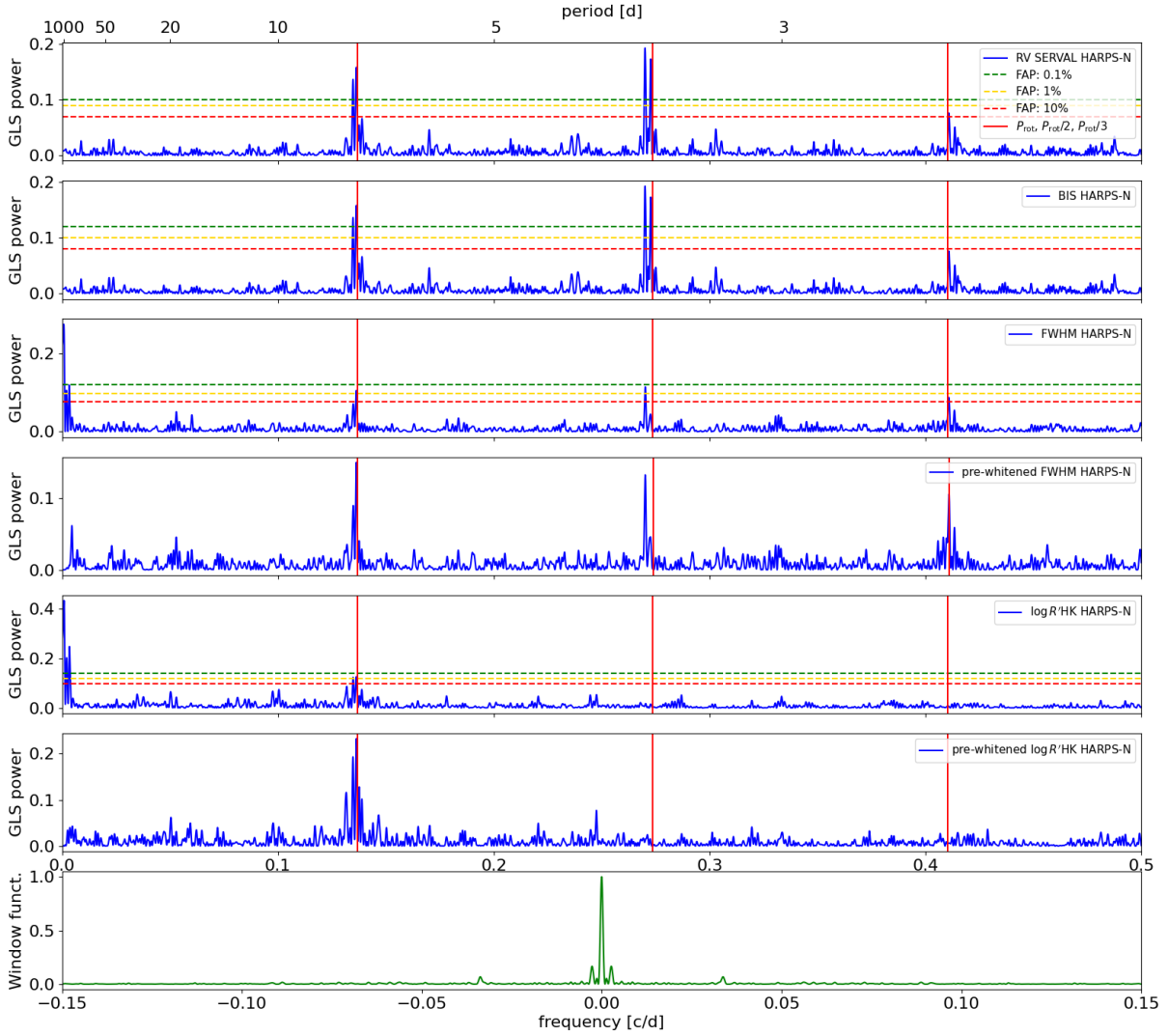


Fig. 4. GLS periodograms of one of the RV dataset (SERVAL, all orders) and stellar activity diagnostics extracted from HARPS-N spectra.

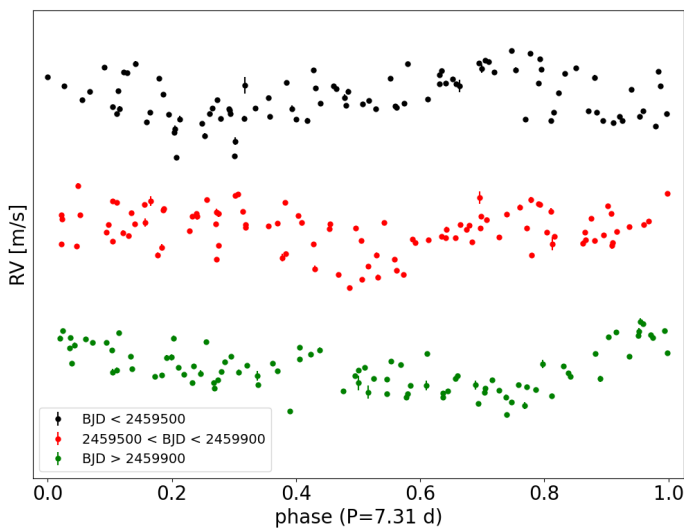


Fig. 5. RVs (SERVAL extraction, wavelength range nr. 3) phase-folded to the stellar rotation period (same epoch used as phase=0 for the three series). Data are divided into three sub-samples (with offsets applied for better readability) to show how the variability due to stellar activity changes on a seasonal basis.

5. Photometric and spectroscopic data modeling

5.1. Transit light curve modeling

In this study, we do not provide additional photometric transits to those that have already been presented and analysed by [Osborn et al. \(2022\)](#) and [Zhang et al. \(2023\)](#). Nonetheless, we performed a fit of all the available TESS, CHEOPS, and LCO/MuSCAT3 transit light curves using our own extracted TESS photometric dataset (Sect. 2.1), and the CHEOPS and LCO/MuSCAT3 detrended light curves published by [Osborn et al. \(2022\)](#).

We modelled the transits using the publicly available code [batman \(Kreidberg 2015\)](#) assuming circular orbits. We explored the full parameter space using the Monte Carlo (MC) nested sampler and Bayesian inference tool [MULTINEST V3.10](#) (e.g. [Feroz et al. 2019](#)), through the [pyMULTINEST](#) wrapper ([Buchner et al. 2014](#)). In place of the ratio between the planetary semi-major axis and the stellar radius a_p/R_* (which is an input parameter required by [batman](#)), we used the stellar density ρ_* as a free parameter of the model (e.g. [Sozzetti et al. 2007](#)). For ρ_* we adopted a Gaussian prior based on the mass and radius derived in Sect. 3, from which we derived the a_p/R_* ratios at each step of the MC sampling. We adopted a quadratic law for the limb darkening (LD) and fitted the coefficients u_1 and

u_2 using the parametrisation and uniform priors for the coefficients q_1 and q_2 given by [Kipping \(2010\)](#) (see Eqs. (15) and (16) therein). We used a different pair of LD coefficients for each telescope. We used uniform priors for the inclination angle of the orbital planes $\mathcal{U}(80,90)$ degrees) and for the relative radius ratios R_p/R_\star ($\mathcal{U}(0,1)$). We included uncorrelated jitter terms and offsets in the model (uniform priors) for each instrument. Following the methodology outlined in [Mantovan et al. \(2022\)](#), we used *Gaia* DR3 data to measure the dilution factor and identified nearby contaminating stars that might be blended with the target. The dilution factor is defined as the total flux from contaminant stars that fall into the photometric aperture divided by the flux of the target star. We found an almost negligible dilution factor (~ 0.0005) for TOI-2076, so low that it was not necessary to correct the planetary radii measurements derived from the fit of the light curves.

Our derived posterior distributions for the planetary radii are shown in Fig. 6, together with those corresponding to the measurements available in the literature. According to our analysis, the planetary radii are $R_b = 2.51 \pm 0.05 R_\oplus$, $R_c = 3.33 \pm 0.07 R_\oplus$, and $R_d = 3.35^{+0.09}_{-0.08} R_\oplus$, for a detrending that employs a sum of sines and cosines, and $R_b = 2.58 \pm 0.05 R_\oplus$, $R_c = 3.37 \pm 0.07 R_\oplus$, and $R_d = 3.22^{+0.09}_{-0.08} R_\oplus$, for a detrending that uses a spline function with a robust Huber estimator. There is an agreement within 1σ between our different measurements. In this work, we take the weighted average of the values as our reference planet radii: $R_b = 2.54 \pm 0.04 R_\oplus$, $R_c = 3.35 \pm 0.05 R_\oplus$, and $R_d = 3.29 \pm 0.06 R_\oplus$. We verified that the radius measurements are not influenced by the presence of TTVs for planets *b* and *c* (of the order of a few minutes), as reported by [Osborn et al. \(2022\)](#). We confirm that all three planets have sub-Neptune sizes and that the innermost planet *b* has the smallest radius. We note that for planet *c*, we find a smaller radius with respect to that measured by [Osborn et al. \(2022\)](#). The values differ at a level of 2.1 and 1.6 σ , depending on the data detrending method. Nonetheless, our analysis includes one more TESS transit with respect to the sample analysed by [Osborn et al. \(2022\)](#).

5.2. RV modelling and planetary mass measurements

We analysed the RVs of TOI-2076 with the goal of measuring the masses of the three planets in the system. We tested several models to try to mitigate the dominant stellar activity signals, all based on Gaussian process (GP) regression (see Appendix B for details). As we discussed in Sect. 4, the RV time series is dominated by periodic signals unambiguously ascribable to stellar activity, thus we adopted GP-based models that include the stellar rotation period, $P_{\text{rot}, \star}$, as a free parameter. We applied each test model to a time series of RVs extracted from HARPS-N spectra using different algorithms, as described in Sect. 2.3. Some of the analysed datasets include all the RVs considered in this study (HARPS-N, CARMENES, and NEID data points), while others are limited to the much larger sample of HARPS-N RVs time series.

Taking into account the large number of test models, RV extraction methods, and free parameters, along with the fact that the expected planetary Doppler semi-amplitudes are at least one order of magnitude lower than the dominant activity scatter, we did not perform a joint RV+transit fit, because the much longer computational time does not give better results. Instead, we used the best-fit transit ephemeris derived in Sect. 5.1 as Gaussian priors for the RV-only modeling. While this approach made our analysis bearable by greatly reducing the computation

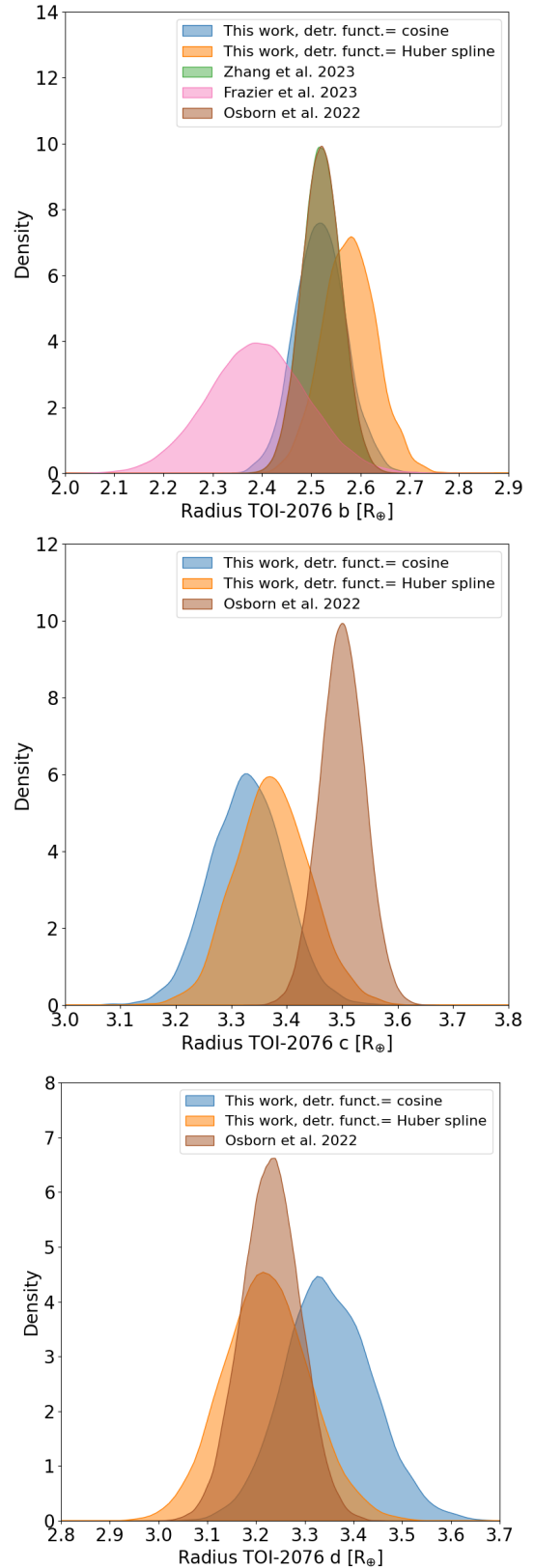


Fig. 6. Posterior distributions of the planetary radii derived from the analysis of the available light curves, which include our version of the TESS light curve, which was detrended using two different algorithms, as described in Sect. 2.1. We also show the posterior distributions corresponding to the radius measurements available in the literature. The posteriors for planet *b* corresponding to the measurements of [Osborn et al. \(2022\)](#) and [Zhang et al. \(2023\)](#) are equal and, therefore, they are not discernible.

Table 3. Summary of the results derived from the mass posterior distributions shown in Fig. 7 and Figs. C.3–C.5, listed according to the HARPS-N RV extraction recipes described in Table 1.

HARPS-N RV dataset	Model-averaged best-fit mass ^(a)	Mean mass upper limit (M_{\oplus}) ^(b)	Mass upper limit rms (M_{\oplus}) ^(b)
<i>TOI-2076 b</i>			
SERVAL, all orders	$3.9^{+2.6}_{-2.3}$	$m_b < 11.4$	1.5
SERVAL, wavelength range nr. 3	$3.8^{+2.6}_{-2.3}$	< 11.2	1.3
DRS, all orders	$3.6^{+2.6}_{-2.1}$	< 10.8	1.2
LBL, all orders	$3.7^{+2.7}_{-2.2}$	< 11.8	1.3
<i>TOI-2076 c</i>			
SERVAL, all orders	$4.0^{+2.9}_{-2.3}$	$m_c < 12.7$	1.1
SERVAL, wavelength range nr. 3	$3.2^{+2.8}_{-2.0}$	< 11.8	0.6
DRS, all orders	$4.0^{+2.9}_{-2.3}$	< 12.8	0.8
LBL, all orders	$3.9^{+3.1}_{-2.4}$	< 13.4	0.6
<i>TOI-2076 d</i>			
SERVAL, all orders	$4.8^{+3.5}_{-2.8}$	$m_d < 15.2$	3.5
SERVAL, wavelength range nr. 3	$7.7^{+3.8}_{-3.7}$	< 18.7	2.0
DRS, all orders	$3.9^{+3.2}_{-2.5}$	< 13.7	3.4
LBL, all orders	$4.3^{+3.6}_{-2.8}$	< 15.2	3.2

Notes. ^(a)Model-averaged values of the 50th percentiles and corresponding error bars. ^(b)Model-averaged values and rms of the planetary mass 3σ upper limits.

time, limiting the modelling to RVs only does not have any significant impact on the results for the dynamical masses in this case.

For each test model, we used MULTINEST to explore the full parameter space and compute the Bayesian evidence $\ln \mathcal{Z}$. The MC set-up included 500 live points, a sampling efficiency of 0.5, and a Bayesian evidence tolerance of 0.3. The GP regression analysis was performed using the publicly available PYTHON module `george` v0.2.1 (Ambikasaran et al. 2015), integrated within the MULTINEST framework. To perform the multi-dimensional GP regression analysis we used the PYTHON module `pyaneti` (Barragán et al. 2019; Barragán et al. 2022a) incorporated into our MULTINEST framework.

For the majority of the tests, we modelled the Doppler signals due to the three planets both with Keplerians and fixing the orbit eccentricities to zero, ignoring terms related to planet-planet interactions. For the orbital ephemeris, we adopted Gaussian priors based on our best-fit solution for the transit light curve modeling. In all the cases, via a model comparison using $\ln \mathcal{Z}$, we found that the models with circular orbits are statistically favoured. Moreover, while still including GP regression, we also performed an RV modeling using the N-body orbital integrator TRANsits and Dynamics of Exoplanetary Systems (TRADES v2.20.0⁶; Borsato et al. 2014). We limited our analysis to the largest dataset represented by the HARPS-N time series to reduce the computational time, with a negligible loss of information. The free parameters related to each planet that we used as input to TRADES are the planet mass, the orbital period, the mean anomaly, the eccentricity, and the argument of periastron. The longitude of the ascending node has been fixed to 180 degrees and the stellar mass has been fixed to the best-fit value derived in our work (0.849 M_{\odot}). In our analysis, TRADES has been incorporated into the MULTINEST+george framework.

⁶ <https://github.com/lucaborsato/trades>

We report in Table B.1 the list of priors used in our analyses. Concerning the results, the GP quasi-periodic regression is able to recover the stellar rotation period with precision level of a hundredth of a day for all the models, using a uniform prior of $\mathcal{U}(0,10)$ days. Examples of the stellar activity term in the RVs, as fitted by our GP regression, are shown in Figs. C.7 and C.8. The median values of the posteriors of the uncorrelated jitter for HARPS-N ($\sigma_{\text{jit, HARPS-N}}$) are generally close to 10 m s^{-1} for all the test models, with the exception of the models based on multi-dimensional GP regression (see Appendix B), for which $\sigma_{\text{jit, HARPS-N}}$ is typically halved.

We show in Fig. 7 the posterior distributions of the planetary masses we obtained for each test model, after selecting one of the different RV extraction methods applied to HARPS-N spectra as an example. Indeed, with a very few noteworthy exceptions, discussed hereafter, the results appear not to be affected by the method used to calculate the HARPS-N RVs. The mass posteriors corresponding to other RV extraction methods are shown in the Appendix (Figs. C.3–C.5). Concerning planet BD+40 2790 b, all the test models do not result in a statistically significant measurement of the mass (e.g. with a significance level of at least 3σ), independently from the considered HARPS-N RV dataset; although we note that all the posteriors do not peak to zero and are generally well matched. Our analysis allowed us to derive 3σ mass upper limits (model-averaged) in the range of ~ 11 – $12 M_{\oplus}$, revealing that BD+40 2790 b is very convincingly less massive than Neptune. A similar conclusion holds for BD+40 2790 c, for which we derived 3σ mass upper limits (model-averaged) in the range ~ 12 – $13.5 M_{\oplus}$. We summarise in Table 3 the values of the model-averaged mass upper limits and the corresponding dispersion. We note that the mass upper limits derived for planet c show the lower dispersion within the different models. We also note that we derived a mass for planet c with a significance level greater than 2σ using a multi-dimensional GP regression trained on the BIS activity indicator (posteriors

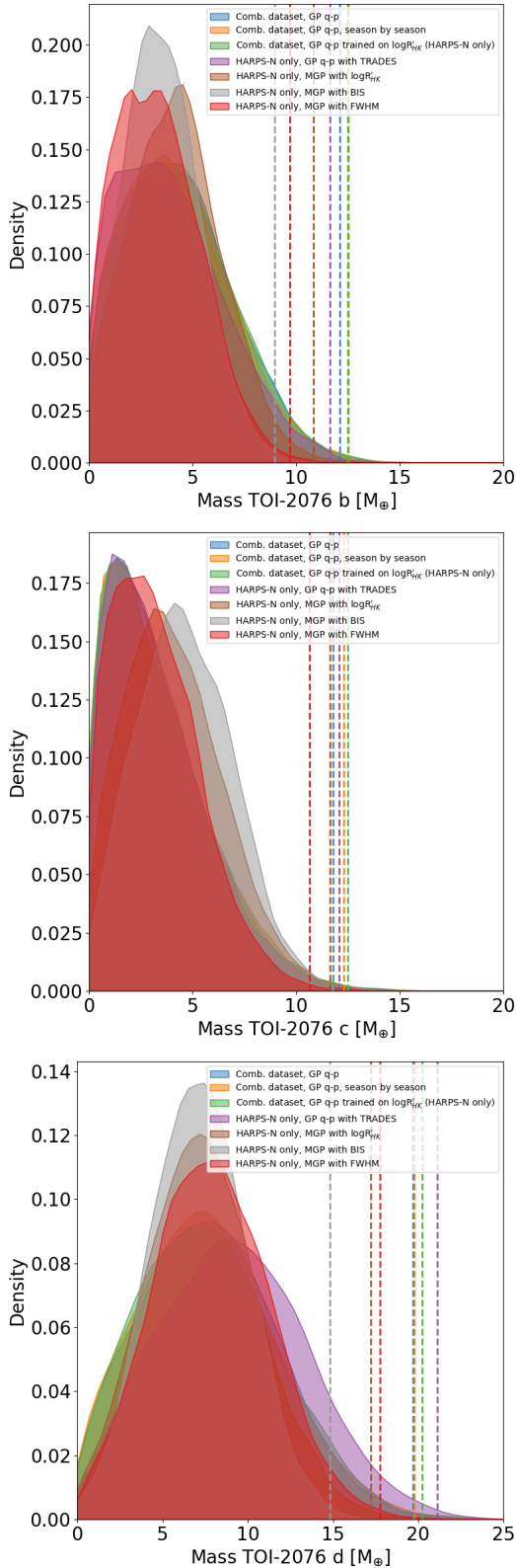


Fig. 7. Posterior mass distributions for the planet BD+40 2790/TOI-2076 b, c, and d (from top to bottom). Here, we show the results corresponding to the HARPS-N RV dataset extracted with SERVAL, wavelength range no. 3. The dashed vertical lines indicate the 3σ upper limits for each distribution with the same colour.

coloured in grey); namely: $m_c = 5.8^{+2.6}_{-2.5}$, $5.7^{+2.5}_{-2.4}$, $5.7^{+2.9}_{-2.6} M_{\oplus}$, for the DRS, SERVAL ‘all echelle orders’, and LBL HARPS-N RV dataset, respectively.

For BD+40 2790 d, we highlight two main results. Using HARPS-N RVs calculated with the DRS, SERVAL ‘all echelle orders’, and LBL pipelines (Fig. C.5), the peaks of the posterior distributions corresponding to the model which uses the N-body orbital integrator TRADES (posteriors coloured in purple) are all shifted toward masses higher than the other models, with the best-fit median values that have a statistical significance in the range of $1.8\text{--}2.1\sigma$ (respectively, $m_d = 7.9 \pm 4.4$, $9.3^{+4.3}_{-4.4}$, and $8.6^{+4.7}_{-4.9} M_{\oplus}$). For the case of HARPS-N RVs calculated with SERVAL in the wavelength range labelled as no. 3 (Table 1), the posterior distribution corresponding to the TRADES-based model does not change significantly ($m_d = 7.9 \pm 4.4 M_{\oplus}$) and the posteriors of all the other test models show a very good agreement (Fig. 7). These outcomes point out that (i) TRADES finds evidence for a value of m_d in the range $\sim 8\text{--}9 M_{\oplus}$ independently of which HARPS-N RV ‘recipe’ is used in the analysis; and (ii) the accordance among different models when using one specific HARPS-N RV dataset may possibly reveal the true mass of BD+40 2790 d. To be conservative, we assume a 3σ upper limit (model-averaged) for the mass of BD+40 2790 d in the range $\sim 14\text{--}19 M_{\oplus}$, with a scatter of $\sim 2\text{--}3.5 M_{\oplus}$ depending on the RV extraction recipe for HARPS-N spectra (Table 3). However, some models provide hints of the true mass of the planet. Looking at the bottom panel of Fig. 7, we note that the models based on a multi-dimensional GP regression provide the most statistically significant mass measurements ($m_d = 7.3^{+3.4}_{-3.2}$, 7.1 ± 2.8 , and $7.8^{+3.5}_{-3.3} M_{\oplus}$, respectively for the models that include $\log R'_{\text{HK}}$, BIS, and FWHM, corresponding to a significance level between $2.3\text{--}2.5\sigma$). In Table 4, we report those of the MGP model that includes the BIS activity diagnostic, as an example of the results obtained for a specific test model.

The observed ‘chromatic’ dependence of the posterior distributions for the mass of planet *d* is interesting. This is confirmed by comparing the results with those of Fig. C.6, which shows the mass posteriors corresponding to HARPS-N RVs extracted with SERVAL in the wavelength ranges 1, 2, and 4, following the nomenclature of Table 1. It would be interesting to confirm this ‘chromatic’ dependence with a spectroscopic follow-up in the near-IR wavelength range.

We note that the models based on multi-dimensional GP regression result with a negative RV acceleration $\dot{\gamma}$; in some cases, with a significance close to 3σ . For instance, in Table 4, we report a result of $\dot{\gamma} \sim -2.63^{+1.06}_{-0.91} \text{ m s}^{-1} \text{ yr}^{-1}$. Given the complexity of the RV modelling presented so far, we do not investigate further the reliability and the nature of this result. Data collected over a longer time baseline could help to test whether a negative $\dot{\gamma}$ is the imprint of a long-term activity trend (which we detected in some of the activity indexes, as discussed in Sect. 4), whether it is due to an outermost companion (noting that Hedges et al. 2021 excluded nearby companions to contrast limits of 5–8 mag using high-resolution imaging), or whether it is an artefact of our test models. We show in Fig. 8 a version of the mass-radius diagram for exoplanets that includes young systems within the age bin 200–400 Myr, wherein TOI-2076 lies. The diagram allows for a comparison of the TOI-2076 system with a sub-sample of older (mature) exoplanets for which precise measurements of mass and radius are currently available.

Table 4. Best-fit values of the free parameters of the model that includes a multi-dimensional GP regression, using the activity diagnostic BIS and the HARPS-N RVs calculated with SERIAL for the wavelength range no. 3 (see Table 1).

Parameter	Best-fit value ^(a)
Multi-dimensional GP parameters:	
A_{RV} ^(b) (m/s)	$3.3^{+1.8}_{-1.4}$
B_{RV} (m/s)	$31.4^{+3.3}_{-2.8}$
A_{BIS} (m/s)	$2.5^{+1.6}_{-1.5}$
B_{BIS} (m/s)	$-33.5^{+1.6}_{-1.5}$
λ (d)	$28.1^{+1.7}_{-1.5}$
w	$0.46^{+0.03}_{-0.02}$
θ (d)	7.33 ± 0.01
Planet-related parameters:	
K_b (m s ⁻¹)	1.1 ± 0.6
Orbital period, P_b (d)	10.35523 ± 0.00001
$T_{conj,b}$ (BJD-2450000)	8950.8289 ± 0.0005
Semi-major axis ^(c) , a_b (au)	0.0880 ± 0.0009
Mass, m_b (M_{\oplus})	3.4 ± 1.8 (<9.0 , 3σ)
Bulk density, ρ_b (g/cm ⁻³)	$1.2^{+0.7}_{-0.6}$
K_c (m s ⁻¹)	1.2 ± 0.6
Orbital period, P_c (d)	21.01549 ± 0.00003
$T_{conj,c}$ (BJD-2450000)	8937.8283 ± 0.0007
Semi-major axis ^(c) , a_c (au)	$0.1411^{+0.0015}_{-0.0014}$
Mass, m_c (M_{\oplus})	4.6 ± 2.3 (<11.8 , 3σ)
Bulk density, ρ_c (g/cm ⁻³)	$0.7^{+0.4}_{-0.3}$
K_d (m s ⁻¹)	1.6 ± 0.6
Orbital period, P_d (d)	35.12551 ± 0.00007
$T_{conj,d}$ (BJD-2450000)	8938.296 ± 0.001
Semi-major axis ^(c) , a_d (au)	$0.1988^{+0.0021}_{-0.0020}$
Mass, m_d (M_{\oplus})	7.3 ± 2.8 (<14.8 , 3σ)
Bulk density, ρ_d (g/cm ⁻³)	$1.1^{+0.5}_{-0.4}$
Acceleration, $\dot{\gamma}$ (m s ⁻¹ d ⁻¹)	$-0.0072^{+0.0029}_{-0.0025}$
RV and BIS-related parameters	
$\sigma_{jit RV, HARPS-N}$ (m s ⁻¹)	$3.9^{+0.8}_{-0.9}$
$\gamma_{RV, HARPS-N}$ (m s ⁻¹)	2.8 ± 0.8
$\sigma_{jit BIS, HARPS-N}$ (m s ⁻¹)	16.2 ± 0.8
$\gamma_{BIS, HARPS-N}$ (m s ⁻¹)	20.8 ± 1.2

Notes. ^(a)The uncertainties are given as the 16th and 84th percentiles of the posterior distributions. For some of the parameters, we provide the 95th percentile in parenthesis. ^(b)The posteriors for A_{RV} , B_{RV} , A_{BIS} , and B_{BIS} are bimodal. A_{RV} and B_{RV} are positively correlated, and we have selected values >0 to calculate the percentiles. A_{BIS} and B_{BIS} are anti-correlated, and we have selected positive values for A_{BIS} and negative values for B_{BIS} to calculate their percentiles. ^(c)We note that our derived semi-major axis values are larger than those reported by Hedges et al. (2021); Osborn et al. (2022), and Zhang et al. (2023); Gaidos et al. (2023) for planet *b*.

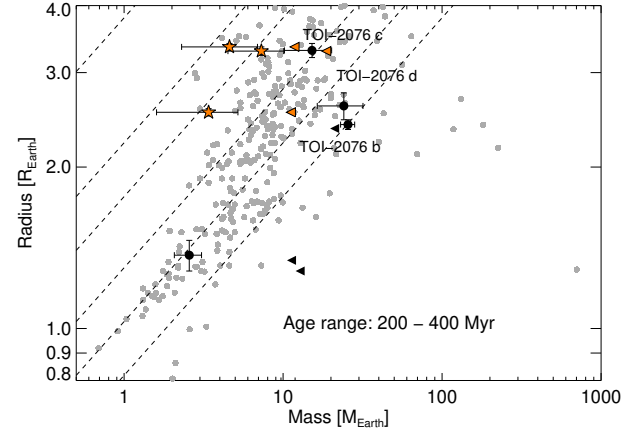


Fig. 8. Mass-radius diagrams showing planets with radius of $R < 4 R_{\oplus}$, and age in the range 200–400 Myr (black symbols), to which TOI-2076 belongs. Black dots indicate planets with a measured mass, while black triangles represent planets for which only a mass upper limit is available. Grey dots represent a sample of older planets with masses and radii known at least at 30 and 10%, respectively. To produce this plot, we considered the known planets collected by the Exo-MerCat tool⁷(Alej et al. 2020, Alej et al. in prep.) by merging the information from the main exoplanets online catalogs (e.g. NASA Exoplanets Archive and Exoplanets Encyclopaedia). The locations of the three planets of the TOI-2076 system are indicated with orange triangles within the appropriate age bin by considering the mass upper limit in Table 3, while the orange star symbols represent the positions of TOI-2076 *b*, *c*, and *d* if we consider the mass obtained with the modelling of the SERIAL RVs (wavelength range no. 3) with a multi-dimensional GP using the BIS. Diagonal dashed lines indicate the location of planets with an equal density.

6. Planetary atmospheric photo-evaporation

We investigated a possible evolution of the planets *b*, *c*, and *d* on the mass-radius parameter space by evaluating the mass loss rate of the planetary atmospheres using the ATES photo-ionisation hydrodynamic code by Caldiroli et al. (2021, 2022), who provided an analytic expression for the planetary mass loss rate. This expression depends on the planetary mean density, gravitational potential energy, and stellar high-energy flux. We also took into account the temporal evolution of all these quantities and, in particular, that of the X-rays and EUV irradiation.

Our code is coupled with the planetary core-envelope model introduced by Lopez & Fortney (2014). This model, developed for H-He dominated atmospheres, provides the envelope radius, R_{env} , as a function of planetary mass, M_p , atmospheric mass fraction, f_{atm} , the stellar bolometric flux incident on the planet, and the age of the system. The model allows us to follow the temporal evolution of the planet’s radius, accounting for the cooling and contraction of the envelope and (indirectly) for the mass loss. Our photo-evaporation code takes into account also the variation of the stellar bolometric flux and effective temperature, computed by means of the MESA Stellar Tracks (MIST; Choi et al. 2016), which are important in determining the planetary radius. This approach was initially introduced by Locci et al. (2019), where population studies were also conducted, and it was subsequently updated for the analysis of individual systems (e.g. Maggio et al. 2022).

For modelling the XUV irradiation at different ages, we adopted two different descriptions (Fig. 9). First, we employed an analytical description as a broken power law of the stellar X-ray

⁷ <https://gitlab.com/eleonoraalei/exo-mercat-gui>

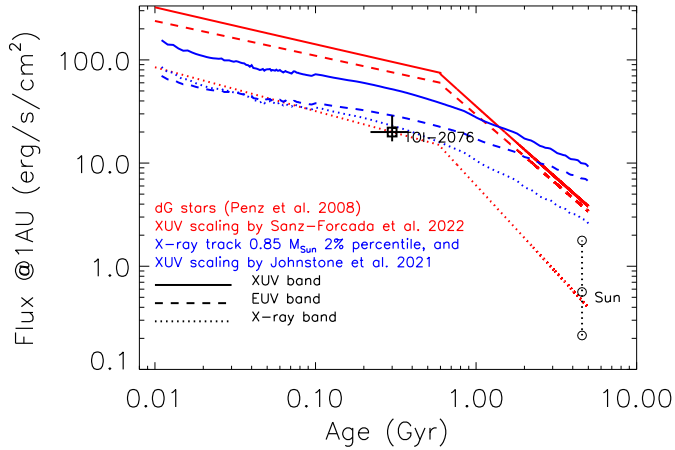


Fig. 9. Temporal evolution of the X-ray (5–100 Å), EUV (100–920 Å), and total XUV flux at 1 AU. The square symbol indicates the X-ray flux of TOI-2076 at the current stellar age. Different evolutionary models and X-ray to EUV scaling laws are compared (see legend).

emission (5–100 Å) versus age (Penz et al. 2008) and we computed the stellar EUV luminosity (100–920 Å), using the scaling law proposed by Sanz-Forcada et al. (2022) (SF22 in the following), which is an updated version of the better-known relation by Sanz-Forcada et al. (2011). Next, we performed simulations, where the evolution of the stellar X-ray and EUV stellar fluxes is described following the semi-empirical approach by Johnstone et al. (2021), which we will refer to as J021 in the following.

Since our analysis of the RVs mainly resulted in the determination of mass upper limits, to simulate the planetary evolution due to photo-evaporation, we explored different sets of possible current masses for each planet below the values reported in Table 3 and down to $4 M_{\oplus}$. Here, we accounted for possible values of the real masses that were not ruled out by our dynamical analysis.

Given the planetary mass and radius, the code first calculates the mass and radius of the core, M_{core} and R_{core} , the radius of the gas envelope, R_{env} , and the atmospheric fraction, f_{atm} . For this aim, we followed the approach in Fernández Fernández et al. (2024) and solved a system of four equations with four unknowns. The unknowns are the four quantities listed above, while the equations include the relation $R_p = R_{\text{core}} + R_{\text{env}}$, an equation linking the planet’s mass to the core mass and atmospheric fraction; $f_{\text{atm}} = M_{\text{env}} / (M_{\text{core}} + M_{\text{env}})$, the equation for calculating the envelope radius proposed by Lopez & Fortney (2014); and an equation proposed by Fortney et al. (2007) that relates the core radius to the core mass; this last equation also allows us to choose between different core compositions, such as a rock and iron or ice and rocky core, with different relative fractions. Once the initial values of the four unknowns are calculated, the simulation begins by evolving the planetary atmosphere over time, as described earlier, keeping fixed the core mass and size, and the star-planet distance as well.

In this study, we investigated the evolutionary history both in the future and in the past, as done, for instance, by Maggio et al. (2022), Damasso et al. (2023), and Mantovan et al. (2024). The simulations start at 10 Myr, when we assume that the protoplanetary disk is fully dissipated and the planets reached their final orbits. They end at 5 Gyr when we assume that the level of stellar activity has decreased to a point where it no longer significantly influences planetary evolution.

The results are shown in Fig. 10, where we present the time evolution of mass, radius, and mass loss rate. The planetary parameters at the current age, at 10 Myr, and at 1 Gyr are also reported in Table C.1 for the two assumed X-EUV scaling laws. In general, we found that all planets behave in the low-gravity regime of the atmospheric hydrodynamic outflow, which occurs when the volume-averaged mean excess energy due to photo-heating exceeds the gravitational binding energy (Caldirola et al. 2022). In this regime, the photo-evaporation efficiency, η , is relatively high, but it never reaches the theoretical energy-limited maximum (Erkaev et al. 2007) due to advective and radiative cooling. Moreover, we verified that the Penz et al. (2008) evolution of the X-ray luminosity, coupled with the SF22 X-EUV scaling law, produces mass loss rates that is a factor of ~ 2 higher than Jo21 at early ages, while the Jo21 approach sustains higher mass loss rates at ages ≥ 1 Gyr. In the following, we describe the case for each planet in more detail.

Planet b. We explored the photo-evaporation history for four possible values of the planetary mass, namely 4, 8, 10, and $12 M_{\oplus}$. We determined the core radii in the range of $R_{\text{core}} = 1.4$ – $1.9 R_{\oplus}$ and atmospheric mass fractions of $f_{\text{env}} \sim 0.8$ – $1.2\% M_p$ at the present age.

The X-ray flux received by the planet is $F_x \sim 2.6 \times 10^3$ erg/s/cm². Assuming the SF22 scaling law, the EUV flux is $F_{\text{EUV}} \sim 9.8 \times 10^3$ erg/s/cm² and the current photo-evaporation rate gives $\dot{M} \sim 2.8 \times 10^{10}$ g/s for the highest mass and $\sim 7.5 \times 10^{10}$ g/s for the lowest mass considered, corresponding to 0.15– $0.22 M_{\oplus}$ /Gyr. Instead, the Jo21 X-EUV relation yields $F_{\text{EUV}} \sim 3.4 \times 10^3$ erg/s/cm² and \dot{M} in the range 1.4 – 4.5×10^{10} g/s, which is a factor of ~ 2 lower than the previous result.

At 10 Myr the photo-evaporation rate was a factor of 5–7 higher, but the total mass lost up to now is $\sim 0.1 M_{\oplus}$ in all cases, and the planet maintained nearly the same core-envelope structure throughout its lifetime. In fact, we found that planet b probably started with a mass $\sim 10\%$ higher than the assumed value and a radius between 3 and $8 R_{\oplus}$, depending on the assumed mass and evolutionary history of the XUV irradiation.

We found that the innermost planet *b* will lose completely its gaseous envelope within the age range 0.5–3 Gyr, unless its mass is very close to the upper limit of $12 M_{\oplus}$.

Observations of absorption in the He I 108.3 nm line were presented by Zhang et al. (2023) and Gaidos et al. (2023) during a single transit of the innermost planet TOI-2076 b, in agreement with the ongoing photo-evaporation predicted by our model. Zhang et al. (2023) presented estimates of the mass loss rate, assuming a mass of $9 M_{\oplus}$ and an XUV flux of 9.5×10^3 erg/cm²/s. They estimated a time scale of 0.6–0.7 Gyr for losing 1% of the planetary mass, which we translate into $\dot{M} = 2.4$ – 2.8×10^{10} g/s, or 0.13– $0.15 M_{\oplus}$ /Gyr. In spite of several differences in the computation⁸, this estimate falls in between the two estimates that we derived assuming the same planetary mass, and the two alternative X-EUV scaling laws. Indeed, we obtained XUV fluxes at the planet from 6.0×10^3 erg/cm²/s (Johnstone et al. 2021) to 1.2×10^4 erg/cm²/s (Sanz-Forcada et al. 2022), that imply mass loss rates from 2.0×10^{10} to 3.7×10^{10} g/s, or 0.1– $0.2 M_{\oplus}$ /Gyr. We conclude that a factor 2 uncertainty in these estimates is a good measure of the systematics in this kind of computation. On the other hand, Gaidos et al. (2023) used the 1-D hydrodynamic escape model of Kubyskhina et al. (2018a,b),

⁸ Zhang et al. (2023) assumed an X-ray luminosity $\sim 20\%$ lower than our estimate, but a higher flux at the planet due to the wrong adoption of a semi-major axis of 0.0631 au for planet *b*.

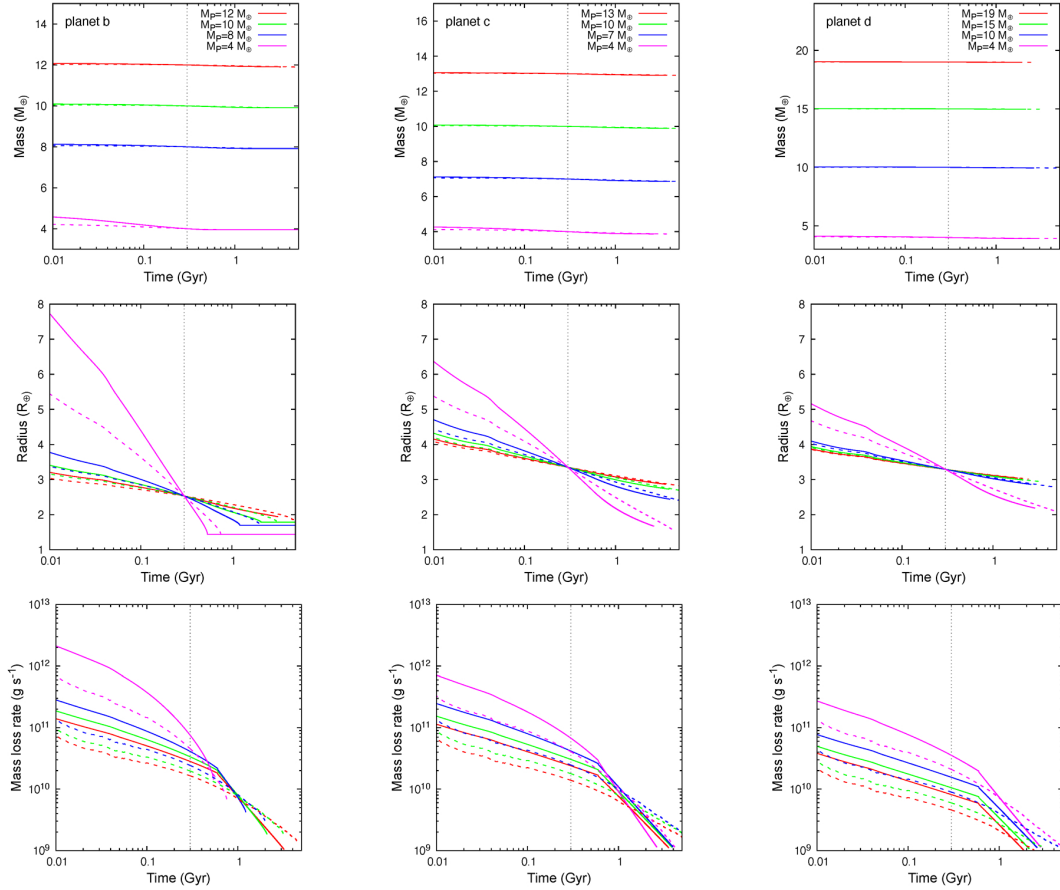


Fig. 10. Temporal evolution of mass, radius, and mass loss rate for three different values of planetary mass for each planet in the TOI-2076 system. The left panels show the evolution of planetary parameters for planet *b*, the middle panels for planet *c*, and the right panel for planet *d*. Solid lines represent models in which we describe the stellar X-ray flux evolution using the law proposed by [Penz et al. \(2008\)](#), and EUV radiation using the law developed by [Sanz-Forcada et al. \(2022\)](#). Dashed lines represent models where the XUV evolution is described using the [Johnstone et al. \(2021\)](#) description. The vertical dotted grey line is located at the current stellar age.

and derived a mass loss rate of $0.77 M_{\oplus}/\text{Gyr}$, assuming a planetary mass of $6.8 M_{\oplus}$ ⁹.

Planet c. We explored four different values for the mass also in this case, but with a slightly larger range: 4, 7, 10, and $13 M_{\oplus}$. Although planet *c* receives a dose of XUV radiation ~ 2.6 times lower than planet *b*, the mass loss rates of the two planets are very similar at any age. This is explained by the lower planetary density of planet *c*, which almost compensates the difference in XUV flux. In fact, the actual mass could be similar to that of planet *b*, but its radius is about 30% larger, which implies a shallower gravitational potential well.

Our model predicts an atmospheric mass fraction $f_{\text{atm}} \sim 3.3\text{--}3.5\%$ at current age, and $\sim 4.2\text{--}9.5\%$ at 10 Myr, assuming SF22, or $3.6\text{--}6.4\%$ following Jo21. The larger value of f_{atm} with respect to planet *b* implies that planet *c* will not lose its atmosphere completely within 5 Gyr.

Planet d. This planet receives an amount of XUV irradiation that is about a factor of 5 lower than planet *b*. We explored a mass range between $4 M_{\oplus}$ and our derived upper limit of $19 M_{\oplus}$. This outermost planet generally shows small variations of mass and radius during the time span of the simulations. For a mass $\sim 19 M_{\oplus}$, this planet remains almost stable against hydrodynamic evaporation, losing only negligible fractions of its envelope due

to hydrostatic Jeans escape. In this case, the planet’s radius evolves only due to the gravitational contraction of the envelope. However, for a mass of $\sim 4 M_{\oplus}$ our model predicts a contraction of $\sim 40\%$ of the planet’s radius up to an age of 5 Gyr.

7. Summary and conclusions

In this work, we used a large dataset of high-precision radial velocities of the ~ 300 Myr old star BD+40 2790 (TOI-2076) with the main goal of measuring the dynamical masses of the three transiting sub-Neptunes discovered around it. The time variations of the RVs are dominated by signals clearly related to the stellar magnetic activity at a level of $\sim 30 \text{ m s}^{-1}$, as it is expected for such a young star. This fact, coupled with the presence of multiple planetary Doppler signals embedded in the data, makes the mass measurements a challenging task. We undertook a complex analysis endeavour, by testing up to seven models in the attempt to filter the activity signals out with different approaches and applying them to HARPS-N RV datasets extracted using four different algorithms, for a total of 28 mass determinations per planet. We considered this approach as one potentially very promising, albeit it is very time consuming because it calls into question two particularly sensitive aspects when dealing with young and active stars with planets which have not been yet investigated for a large sample of targets. However, this same approach can lead to different results

⁹ As in [Zhang et al. \(2023\)](#), we note that they adopted an incorrect orbital semi-major axis in their computation.

that are not straightforward to compare, complicating any final decision on which masses to adopt. Therefore, in this perspective and for the specific case of TOI-2076, we decided that a good way to present our results is by showing all the 28 mass posteriors (Figs. 7 and C.3–C.5) and summarising the measurements as done in Table 3, where the model-averaged values and 3σ upper limits of the planetary masses are listed for each RV extraction algorithm that we tested in this study. For all three planets, none of the best-fit mass measurements reaches a 3σ significance level; therefore our more conservative result is represented by the upper limits. Thus, we can conclude with a high confidence level that the three planets have sub-Neptune masses. On a model-by-model basis, although it is not possible a priori to assume that one model will provide more trustworthy results than others; nonetheless our multi-model approach reveals that in some cases individual posteriors could provide constraints on the masses of the planets better than just 3σ upper limits. For instance, none of the posteriors in Figs. 7 (first and second panel) and C.3–C.4 peaks at null values in all the cases and this suggests that the current masses of planets *b* and *c* could actually be in the range $4\text{--}5 M_{\oplus}$. For the mass of planet *d*, our approach to the data analysis led to the promising value of $\sim 7\text{--}8 M_{\oplus}$, which is a range supported by all the models when we analyse the RVs extracted after excluding some echelle orders at lower wavelengths from the RV computation. For one model in particular, the statistical significance level of the mass goes up to 2.6σ (Table 4). This result would suggest that BD+40 2790 may be a promising target for spectroscopic follow-up in the near-IR for at least confirming the mass of planet *d*; however, for a K-type star such as TOI-2076, the expected RV internal precision attainable with new-generation and high-precision instruments at 4m-class telescopes such as SPIRou (Donati et al. 2020) is lower than that in the optical (Reiners & Zechmeister 2020). Possibly, a TTV follow-up could be a more promising route towards accurate and precise mass measurements. If we assume the results in Table 4 as a reliable characterisation of the system, the three planets could be classified as low-density sub-Neptunes. A comparison with a population of mature planets with similar masses (within the error bars) suggests, in particular, that the radii of planets *b* and *c* are inflated (see the star-like symbols in Fig. 8). Their larger radii could be due to bloated and H-He dominated atmospheres, and, ultimately, to the young age of the system. If so, the current locations of the planets in the mass-radius diagram would be expected to change in the future and move to lower radius values typical of the older population – that is, if their atmospheres will experience mass loss and contraction through photo-evaporation.

In this regard, in the last part of our work we discussed possible evolutionary pathways of the planetary atmospheres by estimating the mass loss rate through photo-evaporation over time, for a grid of possible current masses selected on the base of our derived planetary mass upper limits. Through this theoretical analysis, we derived the predicted values of planetary mass and radius starting from an age of 10 Myr up to a few Gyr. The simulations show that planets *b* and *c* are currently experiencing atmospheric mass loss driven by photo-evaporation and this is a general conclusion that does not depend on their actual masses. We predict for planet *c* an atmospheric mass fraction larger than for planet *b*, along with a mass loss rate that is slightly lower; hence, we expect that the HeI line absorption could be detectable for this planet, similarly to what has been claimed for planet *b*, although the origin of the observed absorption remains controversial (Zhang et al. 2023; Gaidos et al. 2023). We predict that the radius of planet *d* will be reduced for the effects

of to gravitational contraction of the envelope, rather than photo-evaporation mass loss.

Based on the same simulations, we can predict what the locations of each planet in the mass-radius diagram of Fig. 8 could be in the future, as a consequence of size contraction mainly driven by photo-evaporation. For instance, at 5 Gyr from now, the final radius of planet *b* is expected in the range $\sim 1.5\text{--}2 R_{\oplus}$; for planet *c*, the radius should settle within $\sim 2.5\text{--}3 R_{\oplus}$, or to a value lower than $2 R_{\oplus}$ if the mass is $\sim 4 M_{\oplus}$; for planet *d*, the expected final radius should be between $2\text{--}3 R_{\oplus}$. Hence, the predicted final positions are expected to be within the regions occupied by the population of mature exoplanets with similar masses.

With constituent planetary sizes of $R_b = 2.54 \pm 0.04 R_{\oplus}$, $R_c = 3.35 \pm 0.05 R_{\oplus}$, and $R_d = 3.29 \pm 0.06 R_{\oplus}$, as well as period ratios of $P_c/P_b \approx 2.01$ and $P_d/P_c \approx 1.67$, TOI-2076 serves as a prototypical example of the so-called ‘peas-in-a-pod’ configuration. It has been observed that sub-Neptunes orbiting the same star display a striking uniformity in their planetary size, mass, and orbital spacing, such that the overall system architecture resembles peas-in-a-pod (Millholland et al. 2017; Wang 2017; Weiss et al. 2018; Goyal & Wang 2022). It has also been demonstrated that this size uniformity is itself enhanced within systems containing at least one planetary pair close to first-order mean motion resonance (MMR; Goyal et al. 2023). In addition, with the proximity of the inner two planets to the 2:1 MMR, the TOI-2076 system fits well within that framework. Given the especially strong uniformity in planetary size. Additionally, the outer two planets lie close to the 5:3 MMR and harbor nearly identical radii, providing evidence that planetary size uniformity may hold a correspondence with higher-order resonances as well. These highly uniform architectures are believed to emerge as a common and natural consequence of the planetary assembly process, with such possible mechanisms including an energy optimisation of the pairwise planetary mass budget (Adams et al. 2020b; Adams et al. 2020a), construction of close-in resonant chains by a convergent migration process (Terquem & Papaloizou 2007; Morrison et al. 2020; Brož et al. 2021), sequential formation from a narrow planetesimal ring (Batygin & Morbidelli 2023), or planetesimal trapping at disk pressure bumps (Xu & Wang 2024). The vast majority of multi-planet configurations have been observed to harbor non-resonant architectures (Fabrycky et al. 2014), perhaps owing to widespread dynamical instabilities or giant impacts following the disk epoch (Izidoro et al. 2017; Goldberg & Batygin 2022; Lammers et al. 2023), which fully disrupt these resonant chains. As such, it may be the case that near-resonant systems such as TOI-2076 instead experienced a more quiescent evolutionary history, wherein planetary spacing was gently broadened during the disk lifetime (Terquem & Papaloizou 2019; Choksi & Chiang 2020). This may have been the result of stochastic turbulence during migration (Batygin & Adams 2017; Goldberg & Batygin 2023) or secular forcing from a perturbing companion planet (Choksi & Chiang 2023). Accordingly, the absence of large-scale dynamical disruptions may have allowed TOI-2076 to retain a more substantial imprint of its primordial, highly uniform resonant state.

Data availability

RV data are available at the CDS via anonymous ftp to cdsarc.cds.unistra.fr (130.79.128.5) or via <https://cdsarc.cds.unistra.fr/viz-bin/cat/J/A+A/690/A235>

Acknowledgements. This work has been supported by the PRIN-INAF 2019 ‘‘Planetary systems at young ages (PLATEA)’’ and ASI-INAF agreement

no. 2018-16-HH.0. A. Ma. also acknowledges partial support from the PRIN-INAF 2019 “HOT-ATMOS”. We acknowledge financial support from the Agencia Estatal de Investigación of the Ministerio de Ciencia e Innovación MCIN/AEI/10.13039/501100011033 and the ERDF “A way of making Europe” through projects PID2021-125627OB-C32 and PID2022-137241NB-C41, and from the Centre of Excellence “Severo Ochoa” award to the Instituto de Astrofísica de Canarias. S.W. acknowledges support from Heising-Simons Foundation Grant #2023-4050. G.N. thanks for the research funding from the Ministry of Education and Science programme the “Excellence Initiative – Research University” conducted at the Centre of Excellence in Astrophysics and Astrochemistry of the Nicolaus Copernicus University in Toruń, Poland. L.M. acknowledges financial contribution from PRIN MUR 2022 project 2022J4H55R. L.B. and T.Z. acknowledge the support by the CHEOPS ASI-INAF agreement no. 2019-29-HH.0. T.Z. acknowledges NVIDIA Academic Hardware Grant Program for the use of the Titan V GPU card, and the Italian MUR Departments of Excellence grant 2023–2027 “Quantum Frontiers”. This paper contains data taken with the NEID instrument, which was funded by the NASA-NSF Exoplanet Observational Research (NN-EXPLORE) partnership and built by Pennsylvania State University. NEID is installed on the WIYN telescope, which is operated by the National Optical Astronomy Observatory, and the NEID archive is operated by the NASA Exoplanet Science Institute at the California Institute of Technology. NN-EXPLORE is managed by the Jet Propulsion Laboratory, California Institute of Technology under contract with the National Aeronautics and Space Administration. This work has made use of data from the European Space Agency (ESA) mission *Gaia* (<https://www.cosmos.esa.int/gaia>), processed by the *Gaia* Data Processing and Analysis Consortium (DPAC, <https://www.cosmos.esa.int/web/gaia/dpac/consortium>). Funding for the DPAC has been provided by national institutions, in particular the institutions participating in the *Gaia* Multilateral Agreement.

References

- Adams, F. C., Batygin, K., & Bloch, A. M. 2020a, *MNRAS*, **494**, 2289
- Adams, F. C., Batygin, K., Bloch, A. M., & Laughlin, G. 2020b, *MNRAS*, **493**, 5520
- Alei, E., Claudi, R., Bignamini, A., & Molinaro, M. 2020, *Astron. Comput.*, **31**, 100370
- Ambikasaran, S., Foreman-Mackey, D., Greengard, L., Hogg, D. W., & O’Neil, M. 2015, *IEEE Trans. Pattern Anal. Mach. Intell.*, **38**
- Artigau, É., Cadieux, C., Cook, N. J., et al. 2022, *AJ*, **164**, 84
- Baranne, A., Queloz, D., Mayor, M., et al. 1996, *A&AS*, **119**, 373
- Baratella, M., D’Orazi, V., Biazzo, K., et al. 2020a, *A&A*, **640**, A123
- Baratella, M., D’Orazi, V., Carraro, G., et al. 2020b, *A&A*, **634**, A34
- Barragán, O., Gandolfi, D., & Antonucciello, G. 2019, *MNRAS*, **482**, 1017
- Barragán, O., Aigrain, S., Rajpaul, V. M., & Zicher, N. 2022a, *MNRAS*, **509**, 866
- Barragán, O., Armstrong, D. J., Gandolfi, D., et al. 2022b, *MNRAS*, **514**, 1606
- Barragán, O., Gillen, E., Aigrain, S., et al. 2023, *MNRAS*, **522**, 3458
- Baruteau, C., Crida, A., Paardekooper, S. J., et al. 2014, in *Protostars and Planets VI*, eds. H. Beuther, R. S. Klessen, C. P. Dullemond, & T. Henning, 667
- Batygin, K., & Adams, F. C. 2017, *AJ*, **153**, 120
- Batygin, K., & Morbidelli, A. 2023, *Nat. Astron.*, **7**, 330
- Benatti, S., Desidera, S., & GAPS Young Objects Team. 2023a, in *Memorie della Società Astronomica Italiana*, **94**, 195
- Benatti, S., Desidera, S., & Team, G.-Y. 2023b, in *HACK100*, **94**, eds. P. Bonifacio, & P. Molaro, 195
- Biazzo, K., D’Orazi, V., Desidera, S., et al. 2022, *A&A*, **664**, A161
- Borsato, L., Marzari, F., Nascimbeni, V., et al. 2014, *A&A*, **571**, A38
- Bressan, A., Marigo, P., Girardi, L., et al. 2012, *MNRAS*, **427**, 127
- Brewer, J. M., Fischer, D. A., Valenti, J. A., & Piskunov, N. 2016, *ApJS*, **225**, 32
- Brož, M., Chrenko, O., Nesvorný, D., & Dauphas, N. 2021, *Nat. Astron.*, **5**, 898
- Buchner, J., Georgakakis, A., Nandra, K., et al. 2014, *A&A*, **564**, A125
- Butters, O. W., West, R. G., Anderson, D. R., et al. 2010, *A&A*, **520**, L10
- Caldiroli, A., Haardt, F., Gallo, E., et al. 2021, *A&A*, **655**, A30
- Caldiroli, A., Haardt, F., Gallo, E., et al. 2022, *A&A*, **663**, A122
- Cale, B. L., Reefe, M., Plavchan, P., et al. 2021, *AJ*, **162**, 295
- Canocchi, G., Malavolta, L., Pagano, I., et al. 2023, *A&A*, **672**, A144
- Carleo, I., Malavolta, L., Lanza, A. F., et al. 2020, *A&A*, **638**, A5
- Carleo, I., Desidera, S., Nardiello, D., et al. 2021, *A&A*, **645**, A71
- Casagrande, L., Lin, J., Rains, A. D., et al. 2021, *MNRAS*, **507**, 2684
- Castelli, F. & Kurucz, R. L. 2003, in *Modelling of Stellar Atmospheres*, **210**, eds. N. Piskunov, W. W. Weiss, & D. F. Gray, A20
- Chatterjee, S., Ford, E. B., Matsumura, S., & Rasio, F. A. 2008, *ApJ*, **686**, 580
- Choi, J., Dotter, A., Conroy, C., et al. 2016, *ApJ*, **823**, 102
- Choksi, N., & Chiang, E. 2020, *MNRAS*, **495**, 4192
- Choksi, N., & Chiang, E. 2023, *MNRAS*, **522**, 1914
- Cosentino, R., Lovis, C., Pepe, F., et al. 2012, *SPIE Conf. Ser.*, **8446**, 84461V
- Cossou, C., Raymond, S. N., Hersant, F., & Pierens, A. 2014, *A&A*, **569**, A56
- Covino, E., Esposito, M., Barbieri, M., et al. 2013, *A&A*, **554**, A28
- Cutri, R. M., Skrutskie, M. F., van Dyk, S., et al. 2003, *VizieR Online Data Catalog*, II/246
- Cutri, R. M., Wright, E. L., Conrow, T., et al. 2021, *VizieR Online Data Catalog*, II/328
- Damasso, M., Locci, D., Benatti, S., et al. 2023, *A&A*, **672**, A126
- Donati, J. F., Kouach, D., Moutou, C., et al. 2020, *MNRAS*, **498**, 5684
- Dotter, A. 2016, *ApJS*, **222**, 8
- Dutra-Ferreira, L., Pasquini, L., Smiljanic, R., Porto de Mello, G. F., & Steffen, M. 2016, *A&A*, **585**, A75
- Eastman, J. D., Rodriguez, J. E., Agol, E., et al. 2019, arXiv e-prints [arXiv:1907.09480]
- Erkaev, N. V., Kulikov, Y. N., Lammer, H., et al. 2007, *A&A*, **472**, 329
- Fabrycky, D. C., Lissauer, J. J., Ragozzine, D., et al. 2014, *ApJ*, **790**, 146
- Fernández Fernández, J., Wheatley, P. J., King, G. W., & Jenkins, J. S. 2024, *MNRAS*, **527**, 911
- Feroz, F., Hobson, M. P., Cameron, E., & Pettitt, A. N. 2019, *Open J. Astrophys.*, **2**, 10
- Filomeno, S., Biazzo, K., Baratella, M., et al. 2024, *A&A*, in press, <https://doi.org/10.1051/0004-6361/202450611>
- Ford, E. B., & Rasio, F. A. 2008, *ApJ*, **686**, 621
- Fortney, J. J., Marley, M. S., & Barnes, J. W. 2007, *ApJ*, **659**, 1661
- Frazier, R. C., Stefánsson, G., Mahadevan, S., et al. 2023, *ApJ*, **944**, L41
- Gaia Collaboration (Prusti, T., et al.) 2016, *A&A*, **595**, A1
- Gaia Collaboration (Brown, A. G. A., et al.) 2021, *A&A*, **649**, A1
- Gaia Collaboration (Vallenari, A., et al.) 2023, *A&A*, **674**, A1
- Gaidos, E., Hirano, T., Lee, R. A., et al. 2023, *MNRAS*, **518**, 3777
- Gilbertson, C., Ford, E. B., Jones, D. E., & Stenning, D. C. 2020, *ApJ*, **905**, 155
- Goldberg, M., & Batygin, K. 2022, *AJ*, **163**, 201
- Goldberg, M., & Batygin, K. 2023, *ApJ*, **948**, 12
- Goyal, A. V., & Wang, S. 2022, *ApJ*, **933**, 162
- Goyal, A. V., Dai, F., & Wang, S. 2023, *ApJ*, **955**, 118
- Haywood, R. D., Collier Cameron, A., Queloz, D., et al. 2014, *MNRAS*, **443**, 2517
- Hedges, C., Hughes, A., Zhou, G., et al. 2021, *AJ*, **162**, 54
- Hipke, M., David, T. J., Mulders, G. D., & Heller, R. 2019, *AJ*, **158**, 143
- Høg, E., Fabricius, C., Makarov, V. V., et al. 2000, *A&A*, **355**, L27
- Hunter, A., Macgregor, A. B., Szabo, T., Wellington, C., & Bellgard, M. I. 2012, *Source Code Biol. Med.*, **7**, 1
- Izidoro, A., Ogihara, M., Raymond, S. N., et al. 2017, *MNRAS*, **470**, 1750
- Jackson, B., Greenberg, R., & Barnes, R. 2008, *ApJ*, **678**, 1396
- Johnstone, C. P., Bartel, M., & Güdel, M. 2021, *A&A*, **649**, A96
- Kaminski, A., Trifonov, T., Caballero, J. A., et al. 2018, *A&A*, **618**, A115
- Kaplan, K. F., Bender, C. F., Terrien, R. C., et al. 2019, in *Astronomical Society of the Pacific Conference Series*, **523**, *Astronomical Data Analysis Software and Systems XXVII*, eds. P. J. Teuben, M. W. Pound, B. A. Thomas, & E. M. Warner, 567
- Kipping, D. M. 2010, *MNRAS*, **408**, 1758
- Kochanek, C. S., Shappee, B. J., Stanek, K. Z., et al. 2017, *PASP*, **129**, 104502
- Kraus, A. L., Cody, A. M., Covey, K. R., et al. 2015, *ApJ*, **807**, 3
- Kreidberg, L. 2015, *PASP*, **127**, 1161
- Kubyskhina, D., Fossati, L., Erkaev, N. V., et al. 2018a, *ApJ*, **866**, L18
- Kubyskhina, D., Fossati, L., Erkaev, N. V., et al. 2018b, *A&A*, **619**, A151
- Lammers, C., Hadden, S., & Murray, N. 2023, *MNRAS*, **525**, L66
- Lillo-Box, J., Lopez, T. A., Santerne, A., et al. 2020, *A&A*, **640**, A48
- Lind, K., Asplund, M., & Barklem, P. S. 2009, *A&A*, **503**, 541
- Locci, D., Cecchi-Pestellini, C., & Micela, G. 2019, *A&A*, **624**, A101
- Lopez, E. D., & Fortney, J. J. 2014, *ApJ*, **792**, 1
- Maggio, A., Locci, D., Pillitteri, I., et al. 2022, *ApJ*, **925**, 172
- Mahmud, N. I., Crockett, C. J., Johns-Krull, C. M., et al. 2011, *ApJ*, **736**, 123
- Mallorquín, M., Béjar, V. J. S., Lodieu, N., et al. 2023, *A&A*, **671**, A163
- Mamajek, E. E., & Hillenbrand, L. A. 2008, *ApJ*, **687**, 1264
- Mann, A. W., Gaidos, E., Mace, G. N., et al. 2016a, *ApJ*, **818**, 46
- Mann, A. W., Newton, E. R., Rizzuto, A. C., et al. 2016b, *AJ*, **152**, 61
- Mantovan, G., Montalto, M., Piotto, G., et al. 2022, *MNRAS*, **516**, 4432
- Mantovan, G., Malavolta, L., Desidera, S., et al. 2024, *A&A*, **682**, A129
- Millholland, S., Wang, S., & Laughlin, G. 2017, *ApJ*, **849**, L33
- Montalto, M., Piotto, G., Marrese, P. M., et al. 2021, *A&A*, **653**, A98
- Morrison, S. J., Dawson, R. I., & MacDonald, M. 2020, *ApJ*, **904**, 157
- Nardiello, D., Deleuil, M., Mantovan, G., et al. 2021, *MNRAS*, **505**, 3767
- Nardiello, D., Malavolta, L., Desidera, S., et al. 2022, *A&A*, **664**, A163

- Newton, E. R., Mann, A. W., Tofflemire, B. M., et al. 2019, *ApJ*, **880**, L17
- Osborn, H. P., Bonfanti, A., Gandolfi, D., et al. 2022, *A&A*, **664**, A156
- Owen, J. E., & Wu, Y. 2013, *ApJ*, **775**, 105
- Penz, T., Micela, G., & Lammer, H. 2008, *A&A*, **477**, 309
- Pizzolato, N., Maggio, A., Micela, G., Sciortino, S., & Ventura, P. 2003, *A&A*, **397**, 147
- Pollacco, D. L., Skillen, I., Collier Cameron, A., et al. 2006, *PASP*, **118**, 1407
- Prato, L., Huerta, M., Johns-Krull, C. M., et al. 2008, *ApJ*, **687**, L103
- Quirrenbach, A., Amado, P. J., Caballero, J. A., et al. 2014, *SPIE Conf. Ser.*, **9147**, 91471F
- Quirrenbach, A., Amado, P. J., Ribas, I., et al. 2018, *SPIE Conf. Ser.*, **10702**, 107020W
- Rainer, M., Desidera, S., Borsa, F., et al. 2023, *A&A*, **676**, A90
- Rajpaul, V., Aigrain, S., Osborne, M. A., Reece, S., & Roberts, S. 2015, *MNRAS*, **452**, 2269
- Reiners, A., & Zechmeister, M. 2020, *ApJS*, **247**, 11
- Ricker, G. R., Winn, J. N., Vanderspek, R., et al. 2015, *J. Astron. Telescopes Instrum. Syst.*, **1**, 014003
- Roberts, D. H., Lehar, J., & Dreher, J. W. 1987, *AJ*, **93**, 968
- Sanz-Forcada, J., Micela, G., Ribas, I., et al. 2011, *A&A*, **532**, A6
- Sanz-Forcada, J., López-Puertas, M., Nortmann, L., & Lampón, M. 2022, *21st Cambridge Workshop on Cool Stars, Stellar Systems, and the Sun*, https://backoffice.inviteo.com/upload/compte153/Base/inscriptions_projets/fichier/108345-posterjsanzcs21.pdf
- Schwab, C., Rakich, A., Gong, Q., et al. 2016, *SPIE Conf. Ser.*, **9908**, 99087H
- Shappee, B. J., Prieto, J. L., Grupe, D., et al. 2014, *ApJ*, **788**, 48
- Smith, J. C., Stumpe, M. C., Van Cleve, J. E., et al. 2012, *PASP*, **124**, 1000
- Snedden, C. A. 1973, PhD thesis, University of Texas, Austin, USA
- Sousa, S. G., Santos, N. C., Adibekyan, V., Delgado-Mena, E., & Israelian, G. 2015, *A&A*, **577**, A67
- Sozzetti, A., Torres, G., Charbonneau, D., et al. 2007, *ApJ*, **664**, 1190
- Spina, L., Nordlander, T., Casey, A. R., et al. 2020, *ApJ*, **895**, 52
- Stumpe, M. C., Smith, J. C., Van Cleve, J. E., et al. 2012, *PASP*, **124**, 985
- Stumpe, M. C., Smith, J. C., Catanzarite, J. H., et al. 2014, *PASP*, **126**, 100
- Terquem, C., & Papaloizou, J. C. B. 2007, *ApJ*, **654**, 1110
- Terquem, C., & Papaloizou, J. C. B. 2019, *MNRAS*, **482**, 530
- Trifonov, T., Kürster, M., Zechmeister, M., et al. 2018, *A&A*, **609**, A117
- Turrini, D., Marzari, F., Polychroni, D., et al. 2023, *A&A*, **679**, A55
- Van Eylen, V., Albrecht, S., Huang, X., et al. 2019, *AJ*, **157**, 61
- Wang, S. 2017, *RNAAS*, **1**, 26
- Weiss, L. M., Marcy, G. W., Petigura, E. A., et al. 2018, *AJ*, **155**, 48
- Xu, W., & Wang, S. 2024, *ApJ*, **962**, L4
- Yana Galarza, J., Meléndez, J., Lorenzo-Oliveira, D., et al. 2019, *MNRAS*, **490**, L86
- Zakhozhay, O. V., Launhardt, R., Müller, A., et al. 2022, *A&A*, **667**, A63
- Zechmeister, M., & Kürster, M. 2009, *A&A*, **496**, 577
- Zechmeister, M., Reiners, A., Amado, P. J., et al. 2018, *A&A*, **609**, A12
- Zhang, M., Knutson, H. A., Dai, F., et al. 2023, *AJ*, **165**, 62
-
- ¹ INAF – Osservatorio Astrofisico di Torino, Via Osservatorio 20, 10025 Pino Torinese, Italy
 - ² INAF – Osservatorio Astronomico di Palermo, Piazza del Parlamento 1, 90134 Palermo, Italy
 - ³ ESO – European Southern Observatory, Alonso de Cordova 3107, Vitacura, Santiago, Chile
 - ⁴ INAF – Osservatorio Astronomico di Padova, Vicolo dell’Osservatorio 5, 35122 Padova, Italy
 - ⁵ INAF – Osservatorio Astronomico di Roma, Via Frascati 33, 00078 Monte Porzio Catone (Roma), Italy
 - ⁶ Instituto de Astrofísica de Canarias (IAC), Calle Vía Láctea s/n, 38200 La Laguna, Tenerife, Spain
 - ⁷ Departamento de Astrofísica, Universidad de La Laguna (ULL), 38206 La Laguna, Tenerife, Spain
 - ⁸ Department of Astronomy, Indiana University, Bloomington, IN 47405, USA
 - ⁹ Dipartimento di Fisica e Astronomia “G. Galilei” – Università degli Studi di Padova, Vicolo dell’Osservatorio 3, 35122 Padova, Italy
 - ¹⁰ INAF – Osservatorio Astrofisico di Catania, Via S. Sofia 78, 95123 Catania, Italy
 - ¹¹ Institute of Astronomy, Faculty of Physics, Astronomy and Informatics, Nicolaus Copernicus University, Grudziądzka 5, 87–100 Toruń, Poland
 - ¹² INAF – Osservatorio Astronomico di Trieste, via Tiepolo 11, 34143 Trieste, Italy
 - ¹³ INAF – Osservatorio Astronomico di Brera, Via E. Bianchi 46, 23807 Merate (LC), Italy
 - ¹⁴ Fundación Galileo Galilei-IAF, Rambla José Ana Fernández Pérez 7, 38712 Breña Baja, Spain
 - ¹⁵ Dipartimento di Fisica, Università di Roma “Tor Vergata”, Via della Ricerca Scientifica 1, 00133 Rome, Italy
 - ¹⁶ Dipartimento di Fisica, Sapienza Università di Roma, Piazzale Aldo Moro 5, 00185 Roma, Italy
 - ¹⁷ Max Planck Institute for Astronomy, Königstuhl 17, 69117 Heidelberg, Germany
 - ¹⁸ Centro de Astrobiología CSIC-INTA, Carretera de Ajalvir km 4, 28850 Torrejón de Ardoz, Madrid, Spain

Appendix A: Additional spectroscopic data

A.1. CARMENES spectroscopic observations

Between 6 April and 07 October 2021, we collected 22 spectra with the CARMENES spectrograph mounted on the 3.5 m telescope Calar Alto Observatory, Almería, Spain, under the observing programs S21-3.5-006 and F21-3.5-005 (PI Pallé). The exposure time was set to 600s leading to a S/N per pixel of 47–133 at 7370 Å. The CARMENES spectrograph has two arms (Quirrenbach et al. 2014, 2018), the visible (VIS) arm covering the spectral range 5200–9600 Å and a near-infrared (NIR) arm covering the spectral range 9600–17100 Å. CARMENES performance, data reduction and wavelength calibration are described in Trifonov et al. (2018) and Kaminski et al. (2018). Relative radial velocity values, chromatic index (CRX), differential line width (dLW), and H α index values were obtained using *serval* (Zechmeister et al. 2018). All RV measurements were corrected for barycentric motion, secular acceleration and nightly zero-points. In this work, we analysed relative RVs measured from VIS spectra. Their uncertainties are in the range 3.2–10.2 m s⁻¹ with a mean value of 5.7 m s⁻¹.

A.2. NEID spectroscopic observations

NEID is a fiber-fed, red-optical (3800–9300 Å), environmentally stabilized echelle spectrograph (Schwab et al. 2016) installed on the WIYN 3.5 m telescope at Kitt Peak National Observatory. In our study of TOI-2076, we obtained 15 high-resolution observations (resolving power of R ~113,000) using NEID, spanning from May 14 to June 27. Each observation was conducted with an exposure time of 1200 seconds. The data were processed with the updated version 1.2.1 of the NEID Data Reduction Pipeline (DRP; Kaplan et al. 2019), utilising the CCF (Baranne et al. 1996) method to calculate radial velocities (RVs). The NEID CCF RVs from this dataset demonstrated a median single measurement precision of 1.7 m s⁻¹, reflecting a level of accuracy similar to that of HARPS-N.

Appendix B: Description of the test models for RVs and spectroscopic activity diagnostic time series

All our test models to fit the RVs included a component to correct for stellar activity. The signal due to the stellar activity has been fitted through a GP regression adopting a QP kernel, which has been widely and effectively used to mitigate the activity term in the RV time series. We consider this GP kernel an optimal choice in our case, based on the results of the frequency content analysis discussed in Sect. 3.6. A generic element of the QP covariance matrix (e.g. Haywood et al. 2014) is defined as follows:

$$k_{QP}(t, t') = h^2 \cdot \exp \left[-\frac{(t-t')^2}{2\lambda^2} - \frac{\sin^2 \left(\pi(t-t')/\theta \right)}{2w^2} \right] + (\sigma_{RV}^2(t) + \sigma_{jit}^2) \cdot \delta_{t,t'} \quad (B.1)$$

Here, t and t' represent two different epochs of observations, σ_{RV} is the radial velocity uncertainty of a specific instrument, and $\delta_{t,t'}$ is the Kronecker delta. We take other sources of uncorrelated noise – instrumental and/or astrophysical – into account by adding a constant jitter term σ_{jit} for each spectrograph in quadrature to the formal uncertainties σ_{RV} . The GP hyper-parameters are: h , which denotes the scale amplitude of the correlated signal

(specific for each instrument); θ , which represents the periodic timescale of the correlated signal, and corresponds to the stellar rotation period; w , which describes the ‘weight’ of the rotation period harmonic content within a complete stellar rotation (i.e. a low value of w indicates that the periodic variations contain a significant contribution from the harmonics of the rotation periods); and λ , which represents the decay timescale of the correlations and is related to the temporal evolution of the magnetically active regions responsible for the correlated signal observed in the RVs. Hereafter, we provide a description of the different GP-based models used in our work. The priors of the corresponding free (hyper)parameters are listed in Table B.1.

B.1. GP regression not trained on activity indicators

We applied the GP regression to all the available RVs time series (HARPS-N, CARMENES, and NEID). In a first attempt, we used a single QP kernel to model the complete time series, namely, one w and one λ free hyper-parameter was adopted over the whole time span of the data, with one scale amplitude h for each instrument. In a second test, the analysis was performed on a seasonal basis, namely, we divided the dataset into three chunks of time (or ‘seasons’ of BJD 2459068–2459479; 2459571–2459837; 2459950–2460187). We used a triplet of h , w and λ free hyper-parameters to model each chunk of data. We selected this test model taking into account the possibility that the properties of the RV pattern (as seen in the stellar magnetic activity) could change from one season to another.

B.2. GP regression trained on the chromospheric activity diagnostic $\log R'_{HK}$

We used the stellar activity proxy, $\log R'_{HK}$, to help constrain the hyper-parameters of the QP activity component in the full RV time series of HARPS-N. To that purpose, we modelled the $\log R'_{HK}$ time series derived from HARPS-N spectra with a model including a sinusoid to fit the long-term modulation (see Sect. 4), and a QP kernel sharing the w , θ and λ hyper-parameters with the QP kernel used for the GP regression of the HARPS-N RVs (i.e. those GP hyper-parameters are “trained” on the activity diagnostic time series).

B.3. multi-dimensional GP regression

A novel framework to model stellar activity in RV time series simultaneously with activity diagnostics, defined as ‘multi-dimensional GP regression’, was first proposed by Rajpaul et al. (2015) and later further developed by, for instance, Gilbertson et al. (2020) and Barragán et al. (2022a). Within this framework, a set of simultaneous spectroscopic observables derived from the same spectra, containing signals induced by stellar activity, are jointly modelled assuming that they are described by the same underlying function and its derivatives, which are generated by adopting a specific GP kernel. Recently, the multi-dimensional GP regression has been frequently tested as a potentially effective method to measure the masses of planets orbiting active stars, with an age and activity-induced RV scatter comparable to those of TOI-2076 (e.g. Barragán et al. 2022b; Nardiello et al. 2022; Barragán et al. 2023; Damasso et al. 2023). In our study, we adopted the framework detailed in Barragán et al. (2022a) (e.g. see Sect. 3.1 therein for the extensive description of the physical basis of the method and theoretical approach), which

makes use of the first time derivative of a GP-based function. For our analyses, we included in our `MultiNest`-based framework the Python modules specifically developed to perform a multi-dimensional GP regression which are part of the `pyaneti` package¹⁰ (Barragán et al. 2019; Barragán et al. 2022a). We have performed a multi-dimensional GP regression analysis using the HARPS-N RVs and the activity diagnostics $\log R'_{\text{HK}}$, BIS, and FWHM time series derived from the same spectra. We have simultaneously fit the RV dataset with one of the activity indicators at a time (i.e. we performed a two-dimensional GP regression), resulting in three alternative multi-dimensional GP test models. We adopted the QP covariance matrix described in Eq. B as the GP kernel. When $\log R'_{\text{HK}}$ or FWHM was used, we simultaneously fit a sinusoid to model the long-term modulation observed for the two activity indicators (see Sect. 4), and we did not consider the first-time derivative of the GP-based function to model the activity diagnostic time series, following the discussion in Sect. 3 of Rajpaul et al. (2015). In our study, we label with $(A_{\text{RV}}, B_{\text{RV}})$, $(A_{\text{BIS}}, B_{\text{BIS}})$, $A_{\log R'_{\text{HK}}}$, and A_{FWHM} the coefficients that relate the individual time series to the underlying GP-based function (coefficients A) and its first-time derivative (coefficients B). These coefficients are treated as free parameters in our test models. The coefficients of the first-time derivative, $B_{\log R'_{\text{HK}}}$ and B_{FWHM} , are fixed to zero.

Appendix C: Additional plots and tables

¹⁰ <https://github.com/oscaribv/pyaneti>

Table B.1. Prior used to model RVs and spectroscopic activity diagnostics.

Parameter	Prior
<i>GP hyper-parameters:</i>	
$h_{\text{HARPS-N}}$ [m s^{-1}]	$\mathcal{U}(0,100)$
$h_{\text{CARMENES-VIS}}$ [m s^{-1}]	$\mathcal{U}(0,100)$
h_{NEID} [m s^{-1}]	$\mathcal{U}(0,100)$
$\ln \lambda$ [days]	$\mathcal{U}(0,10)$
w	$\mathcal{U}(0,2)$
θ [days]	$\mathcal{U}(0,10)$
<i>Planet-related parameters:</i>	
K_b [m s^{-1}]	$\mathcal{U}(0,20)$
orbital period, P_b [days]	$\mathcal{N}(10.35523, 0.00001)$
$T_{\text{conj, b}}$ [BJD-2450000]	$\mathcal{N}(8950.8289, 0.0005)$
K_c [m s^{-1}]	$\mathcal{U}(0,20)$
orbital period, P_c [days]	$\mathcal{N}(21.01549, 0.00003)$
$T_{\text{conj, c}}$ [BJD-2450000]	$\mathcal{N}(8937.8283, 0.0007)$
K_d [m s^{-1}]	$\mathcal{U}(0,20)$
orbital period, P_d [days]	$\mathcal{N}(35.125514, 0.00007)$
$T_{\text{conj, d}}$ [BJD-2450000]	$\mathcal{N}(8938.2965, 0.001)$
acceleration, $\dot{\gamma}$ [$\text{m s}^{-1} d^{-1}$]	$\mathcal{U}(-1,1)$
<i>activity diagnostic-related parameters:</i>	
semi-amplitude of a long-term activity signal ($\log R'_{\text{HK}}$) [dex]	$\mathcal{U}(0,1)$
semi-amplitude of a long-term activity signal (FWHM) [m/s]	$\mathcal{U}(0,100)$
period of a long-term activity signal ($\log R'_{\text{HK}}$ and FWHM) [days]	$\mathcal{U}(0,2000)$
Reference time of a long-term activity signal ($\log R'_{\text{HK}}$ and FWHM) [BJD-2450000]	$\mathcal{U}(9000, 11000)$
$\sigma_{\text{jit, log } R'_{\text{HK}}}$ [dex]	$\mathcal{U}(0,0.1)$
offset, $\gamma_{\log R'_{\text{HK}}}$ [dex]	$\mathcal{U}(-4.6, -4)$
$\sigma_{\text{jit, FWHM}}$ [m/s]	$\mathcal{U}(0,50)$
offset, γ_{FWHM} [m/s]	$\mathcal{U}(8000, 9500)$
<i>multi-dimensional GP-related parameters:</i>	
$A_{\text{RV}}, B_{\text{RV}}$ [m/s]	$\mathcal{U}(-100, 100)$
$A_{\text{BIS}}, B_{\text{BIS}}$ [m/s]	$\mathcal{U}(-100, 100)$
A_{FWHM} [m/s]	$\mathcal{U}(-100, 100)$
$A_{\log R'_{\text{HK}}}$ [dex]	$\mathcal{U}(-0.1, 0.1)$
<i>Instrument-related parameters:</i>	
$\sigma_{\text{jit, HARPS-N}}$ [m s^{-1}]	$\mathcal{U}(0,50)$ (all RV extractions)
offset, $\gamma_{\text{HARPS-N}}$ [m s^{-1}]	$\mathcal{U}(-13000, -12500)$ (DRS)
offset, $\gamma_{\text{HARPS-N}}$ [m s^{-1}]	$\mathcal{U}(-100, 100)$ (SERVAL)
offset, $\gamma_{\text{HARPS-N}}$ [m s^{-1}]	$\mathcal{U}(-12700, -12300)$ (LBL)
$\sigma_{\text{jit, CARMENES-VIS}}$ [m s^{-1}]	$\mathcal{U}(0,50)$
$\gamma_{\text{CARMENES-VIS}}$ [m s^{-1}]	$\mathcal{U}(-100, 100)$
$\sigma_{\text{jit, NEID}}$ [m s^{-1}]	$\mathcal{U}(0,50)$
γ_{NEID} [m s^{-1}]	$\mathcal{U}(-12800, -12600)$
<i>TRADES specific parameters:</i>	
planet mass [M_{\odot}]	$\mathcal{U}(0, 0.0003)^{(a)}$
planet eccentricity	$\mathcal{N}(0, 0.1)^{(b)}$
argument of periastron [deg]	$\mathcal{U}(0, 360)^{(a)}$
mean anomaly [deg]	$\mathcal{U}(0, 360)^{(a)}$
stellar mass [M_{\odot}]	0.849 (fixed)
longitude of ascending node [deg]	180 (fixed)

^(a) Same prior adopted for all the transiting planets in the system.

^(b) Following the result of Van Eylen et al. (2019) for multi-planet systems. Only positive values were sampled. The same prior has been adopted for all three transiting planets in the system.

Table C.1. Results of the photo-evaporation modeling, assuming two different X-rays and EUV stellar flux evolution models.

X-rays and EUV radiation evolution model: Penz et al. (2008) and Sanz-Forcada et al. (2022)													
Core Radius (R_{\oplus})	Core Mass (M_{\oplus})	Mass (M_{\oplus})	Radius (R_{\oplus})	f_{am} (%)	mass loss rate (g/s)	at 10 Myr			at 1 Gyr				
						Mass (M_{\oplus})	Radius (R_{\oplus})	f_{am} (%)	mass loss rate (g/s)	Mass (M_{\oplus})	Radius (R_{\oplus})	f_{am} (%)	mass loss rate (g/s)
Planet b													
1.9	11.9	12.0	2.54	0.8	2.8×10^{10}	12.10	3.2	1.4	1.4×10^{11}	11.9	2.2	0.3	7.6×10^9
1.8	9.9	10.0	2.54	0.9	3.3×10^{10}	10.10	3.4	1.8	1.9×10^{11}	9.9	2.1	0.2	7.9×10^9
1.7	7.9	8.0	2.54	1.0	4.1×10^{10}	8.10	3.8	2.6	2.8×10^{11}	7.9	1.9	8.4×10^{-2}	7.3×10^9
1.4	3.9	4.0	2.54	1.2	7.5×10^{10}	4.60	7.7	13.6	2.1×10^{12}	3.95	1.4	0.0	0.0
Planet c													
1.9	12.6	13.0	3.35	3.3	2.4×10^{10}	13.10	4.2	3.8	1.1×10^{11}	12.9	3.1	2.9	7.6×10^9
1.8	9.7	10.0	3.35	3.4	3.0×10^{10}	10.10	4.3	4.2	1.5×10^{11}	9.9	3.0	2.8	9.2×10^9
1.6	6.8	7.0	3.35	3.5	4.2×10^{10}	7.10	4.7	5.1	2.5×10^{11}	6.9	2.8	2.3	1.1×10^{10}
1.4	3.9	4.0	3.35	3.5	6.7×10^{10}	4.26	6.4	9.5	7.1×10^{11}	3.9	2.2	0.9	9.1×10^9
Planet d													
2.0	18.5	19.0	3.29	3.0	0.8×10^{10}	19.02	3.8	3.1	3.8×10^{10}	19.0	3.1	2.9	2.6×10^9
1.9	14.5	15.0	3.29	3.2	1.1×10^{10}	15.03	3.9	3.4	5.0×10^{10}	15.0	3.1	3.0	3.4×10^9
1.8	9.7	10.0	3.29	3.4	1.2×10^{10}	10.04	4.1	3.8	7.7×10^{10}	10.0	3.0	3.0	4.9×10^9
1.4	3.9	4.0	3.29	3.4	3.5×10^{10}	4.10	5.2	6.1	2.7×10^{11}	3.9	2.6	1.8	7.4×10^9
X-rays and EUV radiation evolution model: Johnstone et al. (2021)													
Core Radius (R_{\oplus})	Core Mass (M_{\oplus})	Mass (M_{\oplus})	Radius (R_{\oplus})	f_{am} (%)	mass loss rate (g/s)	at 10 Myr			at 1 Gyr				
						Mass (M_{\oplus})	Radius (R_{\oplus})	f_{am} (%)	mass loss rate (g/s)	Mass (M_{\oplus})	Radius (R_{\oplus})	f_{am} (%)	mass loss rate (g/s)
Planet b													
1.9	11.9	12.0	2.54	0.8	2.8×10^{10}	12.10	3.2	1.4	1.4×10^{11}	12.0	2.3	0.5	6.9×10^9
1.8	9.9	10.0	2.54	0.9	2.0×10^{10}	10.0	3.2	1.4	9.8×10^{10}	10.0	2.2	0.4	7.6×10^9
1.7	7.9	8.0	2.54	1.0	2.4×10^{10}	8.10	3.4	1.8	1.4×10^{11}	7.9	2.1	0.4	8.9×10^9
1.4	3.9	4.0	2.54	1.2	4.5×10^{10}	4.20	5.4	6.2	7.1×10^{11}	3.95	1.44	0.0	0.0
Planet c													
1.9	12.6	13.0	3.35	3.3	1.4×10^{10}	13.0	4.1	3.6	6.7×10^{10}	13.0	3.1	3.1	6.3×10^9
1.8	9.7	10.0	3.35	3.4	1.8×10^{10}	10.0	4.2	3.8	8.9×10^{10}	10.0	3.1	3.0	7.8×10^9
1.6	6.8	7.0	3.35	3.5	2.5×10^{10}	7.10	4.4	4.3	1.4×10^{11}	6.9	2.9	2.7	9.8×10^9
1.4	3.9	4.0	3.35	3.5	4.1×10^{10}	4.13	5.4	6.4	3.4×10^{11}	3.9	2.5	1.6	1.1×10^{10}
Planet d													
2.0	18.5	19.0	3.29	3.0	4.5×10^9	19.0	3.8	3.1	2.2×10^{10}	19.0	3.1	3.0	2.1×10^9
1.9	14.5	15.0	3.29	3.2	6.0×10^9	15.0	3.9	3.3	2.9×10^{10}	15.0	3.1	3.1	2.7×10^9
1.8	9.7	10.0	3.29	3.4	8.9×10^9	10.0	4.0	3.7	4.5×10^{10}	10.0	3.1	3.2	4.0×10^9
1.4	3.9	4.0	3.29	3.4	2.1×10^{10}	4.05	4.7	6.1	1.4×10^{11}	4.0	2.7	2.4	7.2×10^9

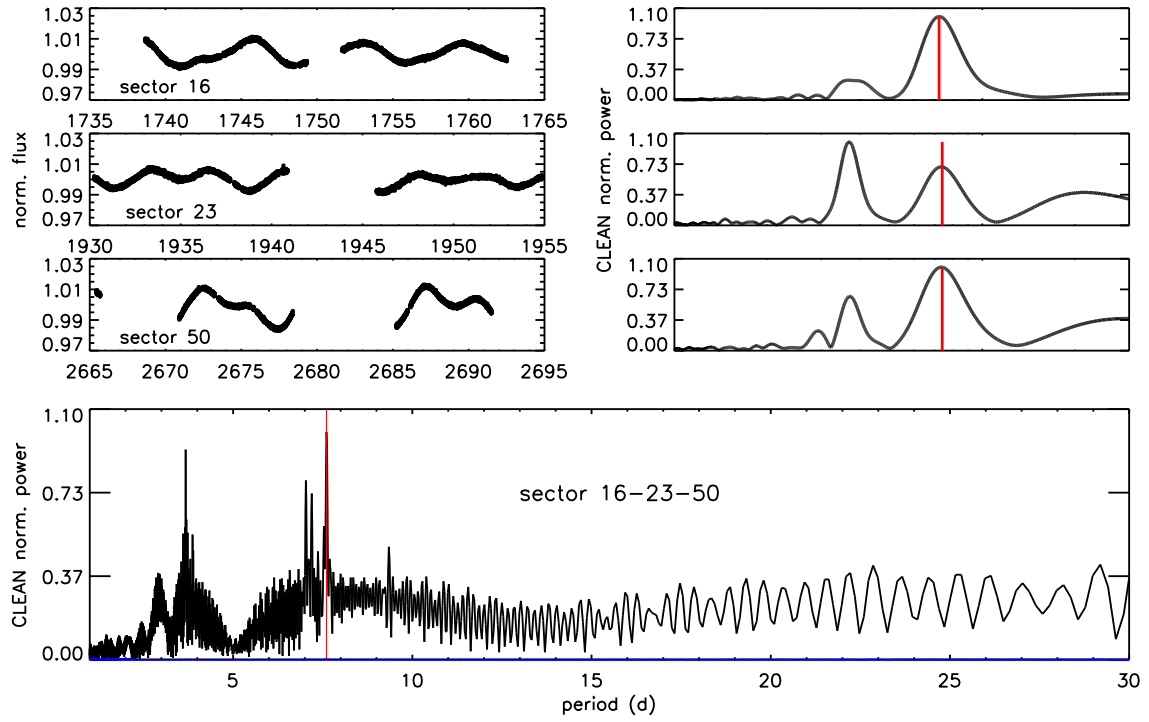


Fig. C.1. Periodograms of the TESS light curve calculated with the CLEAN algorithm.

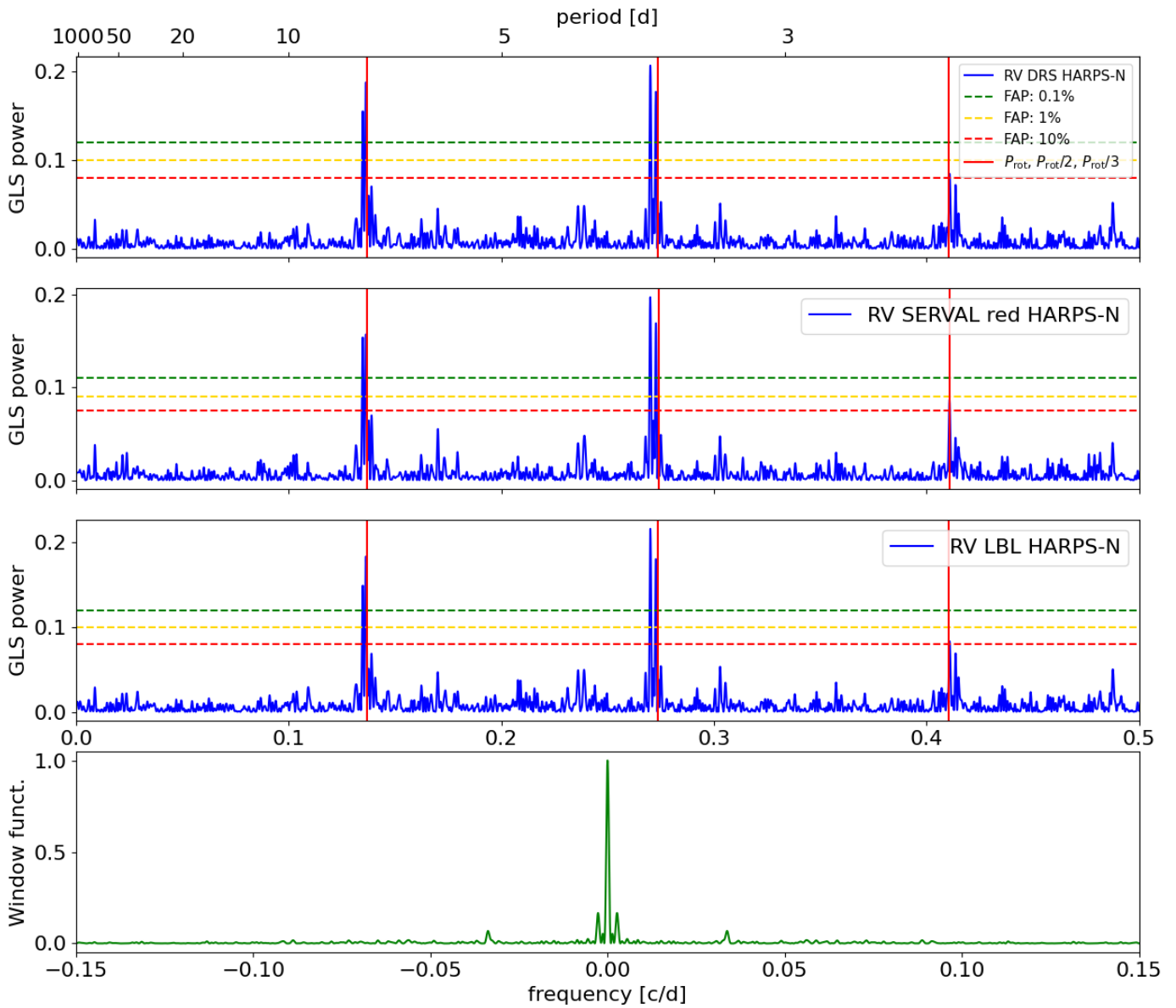


Fig. C.2. GLS periodograms of the RV dataset extracted from HARPS-N spectra using different algorithms, except that shown in Fig. 4 (see Table 1).

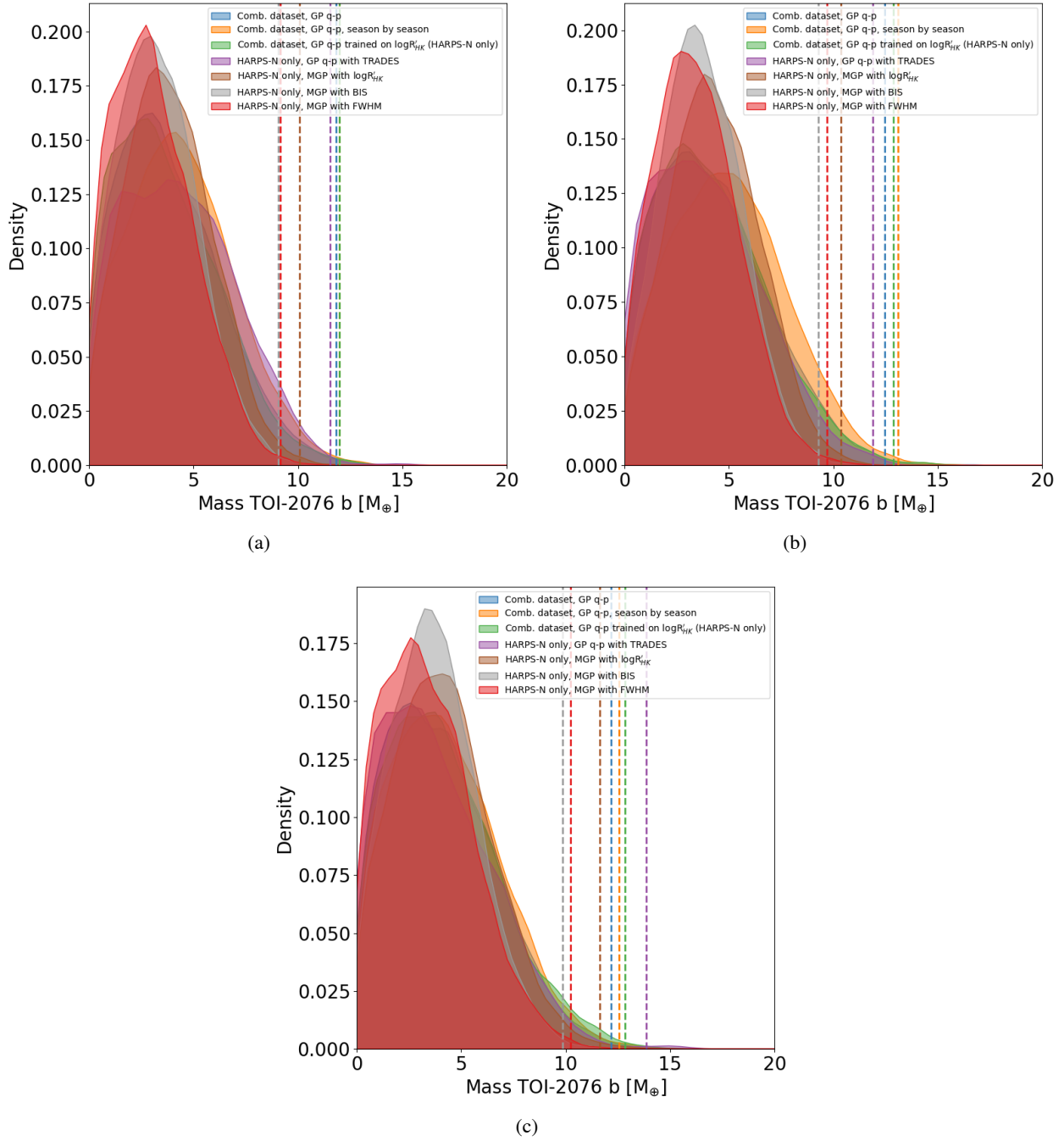


Fig. C.3. Posterior mass distributions for the planet BD+40 2790/TOI-2076 b. The dashed vertical lines indicate the 3σ upper limits for each distribution. Each panel corresponds to a HARPS-N RV dataset extracted with a different method (see Table 1): (a) DRS; (b) SERVAL; (c) LBL

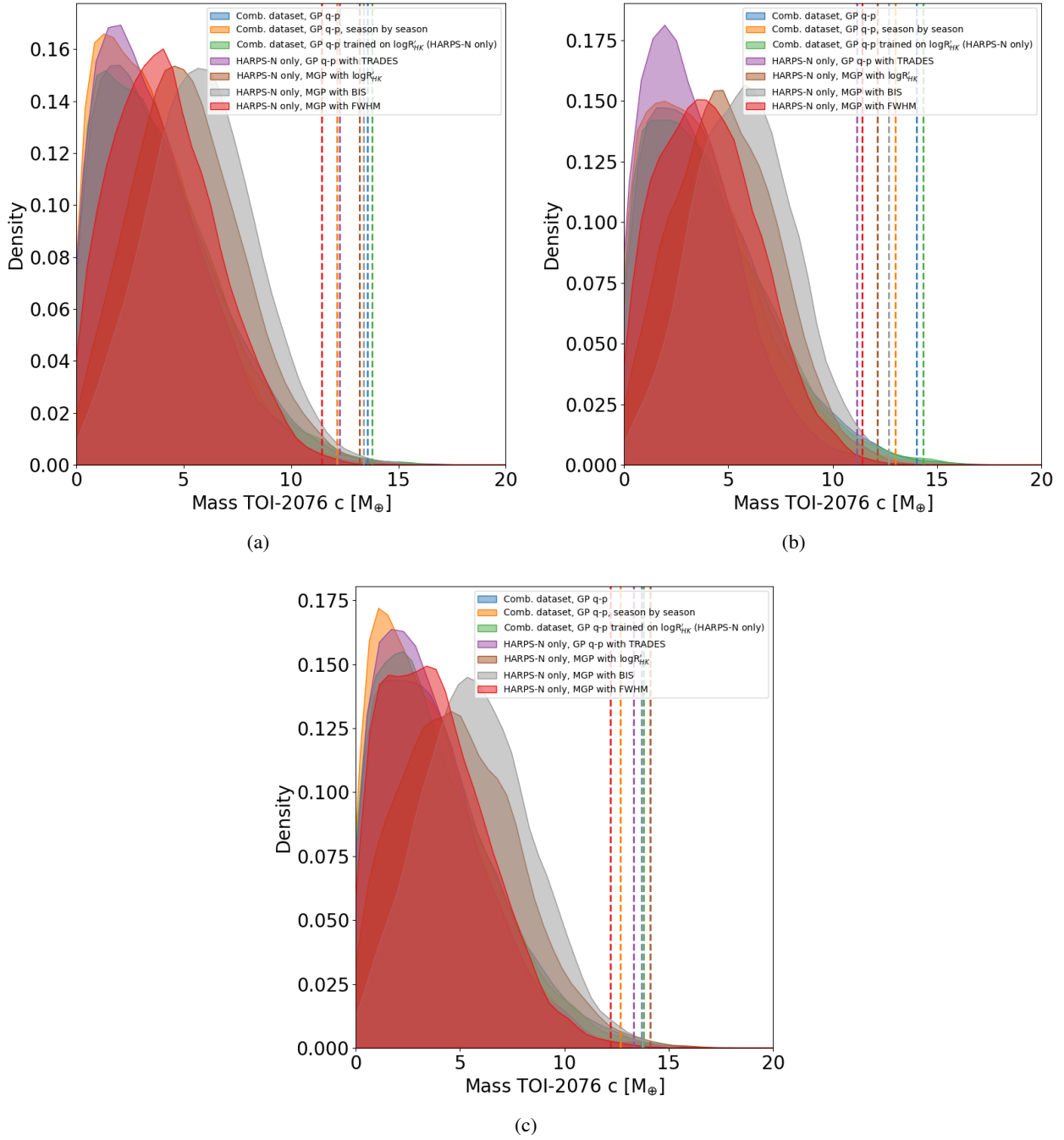


Fig. C.4. Same as in Fig. C.3 but for planet BD+40 2790/TOI-2076 c.

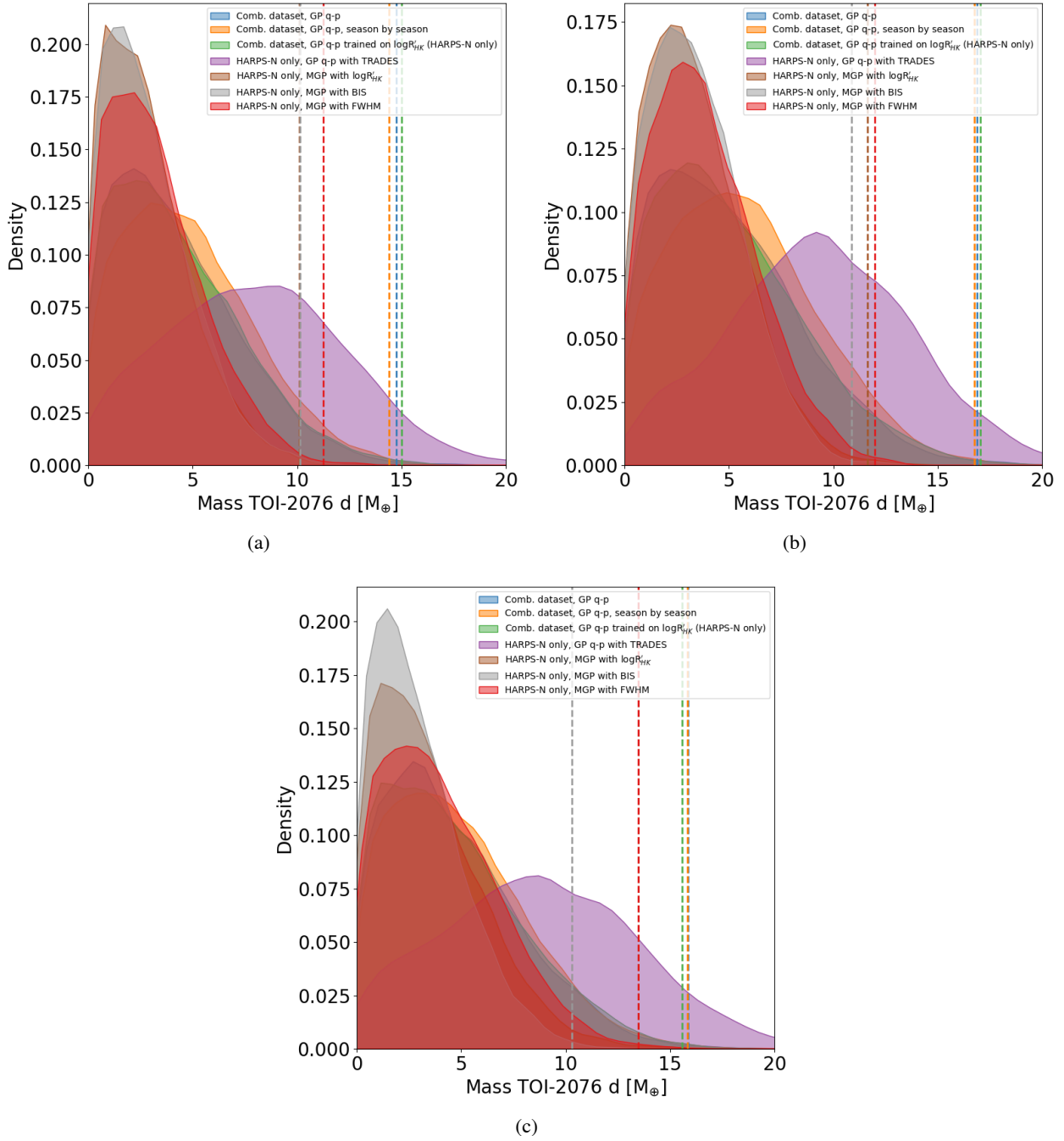
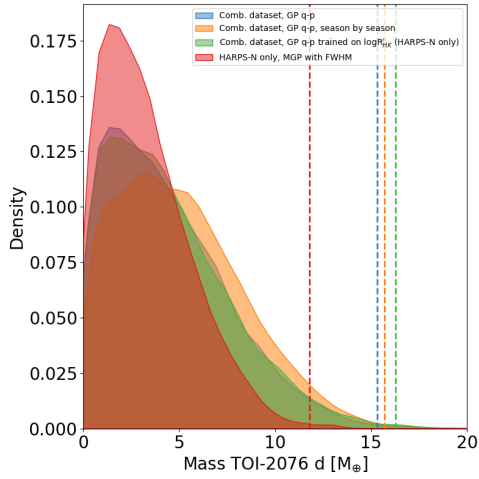
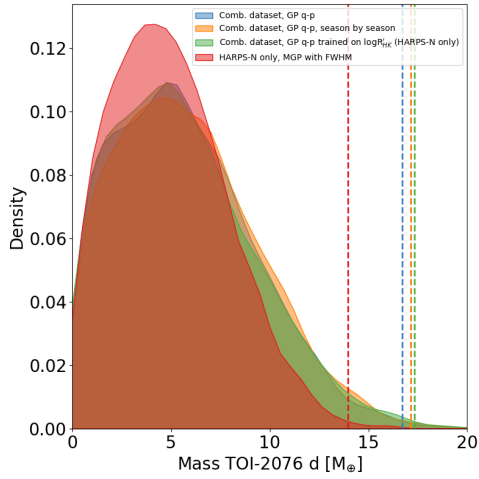


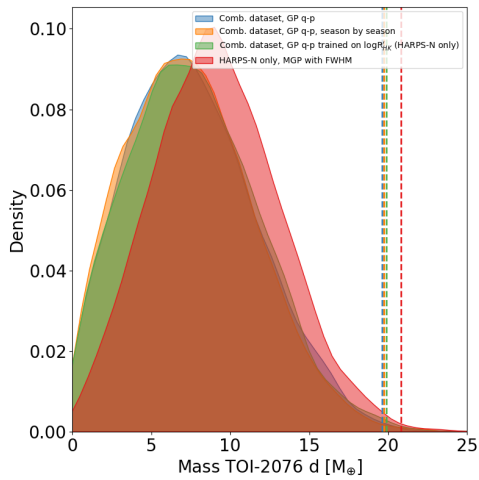
Fig. C.5. Same as in Fig. C.3 but for planet BD+40 2790/TOI-2076 d.



(a)



(b)



(c)

Fig. C.6. Posterior mass distributions for the planet BD+40 2790/TOI-2076 d. The dashed vertical lines indicate the 3σ upper limits for each distribution. Each panel corresponds to a HARPS-N RV dataset extracted with a different method (Table 1): (a) SERVAL, wavelength range nr. 1; (b) SERVAL, wavelength range nr. 2; (c) SERVAL, wavelength range nr. 4.

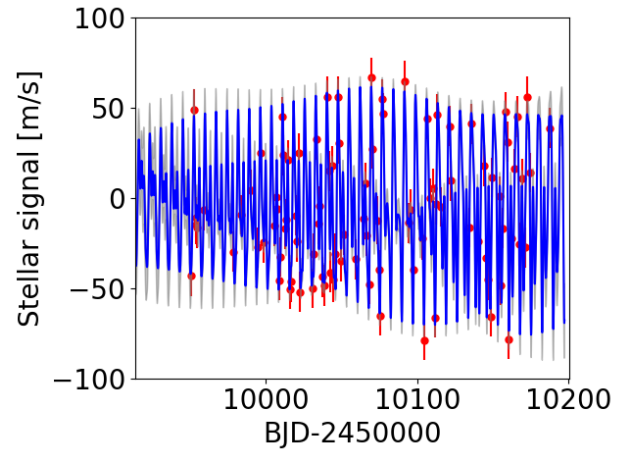
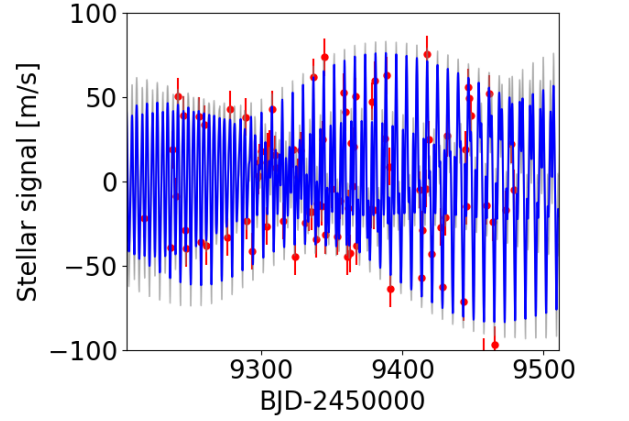


Fig. C.7. Examples of the stellar activity component in the HARPS-N RV time series (SERVAL, all echelle orders) as fitted through a GP regression using a quasi-periodic kernel (the first and third observing season are shown). The curve in blue represents the GP best-fit model; the grey area is 1σ confidence interval. The RV error bars include a jitter term (11 m s^{-1}) added in quadrature to the measurement uncertainties.

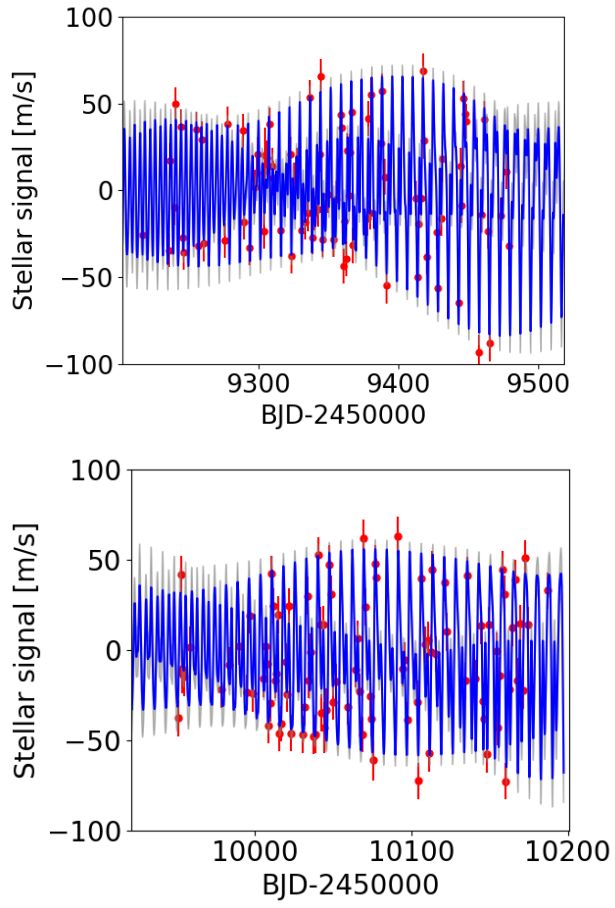


Fig. C.8. Same as in Fig. C.7, but for the HARPS-N RV time series extracted with SERVAL in the wavelength range nr. 3 (Table 1). The RV error bars include a jitter term (9.7 m s^{-1}) added in quadrature to the measurement uncertainties.